

Ionospheric Effects of Rocket Exhaust Products (HEAO-C, Skylab and SPS-HLLV)

October 1980

Prepared for:
U.S. Department of Energy
Office of Energy Research
Satellite Power System Project Division
Washington, D.C. 20585

Prepared by:
Los Alamos Scientific Laboratory
Los Alamos, NM 87545
Under Contract No. W-7405-ENG. 36

DOE/NASA
Satellite Power System
Concept Development and
Evaluation Program

CONTENTS

	<u>Page</u>
ABSTRACT	1
INTRODUCTION	1
BACKGROUND	2
SKYLAB 1 LAUNCH	5
HEAO-C LAUNCH	7
HLLV COMPUTATIONS	16
THE COMPUTER MODEL	19
CONCLUSIONS	21
APPENDIX A-CHEMICAL REACTIONS IN THE TWO-DIMENSIONAL IONOSPHERIC MODEL	22
APPENDIX B- THE TRANSPORT EQUATIONS	24
REFERENCES	30

by

John Zinn, C. Dexter Sutherland, Sidney N. Stone, and Lewis M. Duncan, LASL;
and Richard Behnke, Arecibo Observatory, Arecibo, Puerto Rico

ABSTRACT

This paper reviews the current state of our understanding of the problem of ionospheric F-layer depletions produced by chemical effects of the exhaust gases from large rockets, with particular emphasis on the "Heavy Lift Launch Vehicles" (HLLV) proposed for use in the construction of solar power satellites. The currently planned HLLV flight profile calls for main second-stage propulsion confined to altitudes below 124 km, and a brief orbit-circularization maneuver at apogee. The second-stage engines deposit 9×10^{31} H₂O and H₂ molecules between 56 and 124 km. Model computations show that they diffuse gradually into the ionospheric F region, where they lead to weak but widespread and persistent depletions of ionization and continuous production of H atoms. The orbit-circularization burn deposits 9×10^{29} exhaust molecules at about 480-km altitude. These react rapidly with the F2 region O⁺ ions, leading to a substantial (factor-of-three) reduction in plasma density, which extends over a 1000- by 2000-km region and persists for four to five hours.

Also described are experimental airglow and incoherent-scatter radar measurements performed in conjunction with the 1979 launch of satellite HEAO-C, together with prelaunch and post-launch computations of the ionospheric effects. Several improvements in the model have been driven by the experimental observations. The computer model is described in some detail.

I. INTRODUCTION

Present understanding of ionospheric F-layer depletions caused by exhaust products from large rockets began with the observations by M. Mendillo et al.¹ of an abrupt decrease in vertical electron column density along the trajectory of the launch of Skylab I, May 14, 1973. The effect was attributed¹⁻⁴ to the chemical reaction of rocket exhaust molecules, primarily H₂O and H₂, with O⁺,

the dominant F2-layer ion. These reactions produce molecular ions H₂O⁺, H₃O⁺, and OH⁺, which recombine rapidly with electrons, causing a reduction in electron-ion concentrations.

Practical interest in these ionospheric depletions ("holes") has increased with the advent of proposals to build large space structures in earth orbit, such as the solar power satellite (SPS). Current SPS system studies call for space

transportation activities on a far larger scale than any carried out heretofore. The proposed primary cargo vehicle, called the "heavy lift launch vehicle" (HLLV), is approximately six times larger than the NASA space shuttle vehicle (see, for example, the NASA SPS Concept Evaluation document⁵), and HLLV launches would occur with a frequency of several per day. The present paper is concerned with prediction of the ionospheric and environmental effects of HLLV launches.

According to current design studies,⁵ the HLLV will be a two-stage vehicle with the capability of second-stage flyback. It is to be used for transportation between the surface and a low-earth orbit (LEO) at 450- to 500-km altitude. The second-stage engines are to be fueled with 300 metric tons of liquid hydrogen and 2000 tons of liquid oxygen. Hence, the exhaust gases will consist primarily of H₂O and H₂ in the molar ratio 3:1, about 9×10^{31} molecules in all.

Present launch plans, designed in part to minimize F-layer depletion effects, call for ignition of the second-stage engines at 56-km altitude and engine shutdown with orbital insertion at 108 km, after descent from an intermediate apogee at 123 km. This launch trajectory⁵ leads to an eccentric initial orbit with an apogee at about 480 km. Upon arrival at apogee, the vehicle executes a circularization maneuver, involving the burning of 21 metric tons of propellant and emission of 9×10^{29} exhaust molecules. Upon completion of its mission in LEO, the HLLV returns to earth. The deorbit maneuver requires 11 tons of propellant and emission of 5×10^{29} exhaust molecules.

It is interesting, if not altogether relevant, to note that the number of exhaust molecules from a single HLLV, about 10^{32} , is similar to the total number of electron-ion pairs in the global ionosphere, again about 10^{32} . Since each H₂O molecule is capable, under proper circumstances, of destroying two ion pairs, the effect of one HLLV is potentially large. Fortunately, those circumstances are seldom met.

In previous papers^{6,7} we examined the conditions that determine the "chemical efficiencies" of exhaust molecules for destroying F-layer ions. Further details are described here. We also discuss some additional upper-atmospheric

effects of rocket exhausts, including the production of high-altitude contrails, atomic hydrogen, and airglow. We will describe the current version of an evolving two-dimensional ionospheric computer model and the process of validation of this model by comparisons with experimental observations of the launch effect of Skylab (May 1973) and HEAO-C (September 1979). Our own experimental data on the HEAO-C launch will be described. Finally, the computer model will be applied to the prediction of effects of a single launch of the HLLV.

II. BACKGROUND

Observations of the creation of a large ionospheric hole by the launch of Skylab I (Saturn V rocket launch, 1230 EST, May 14, 1973) were reported by M. Mendillo et al.^{1,2} The ionospheric electron column density was observed to be reduced by 50% or more over a period commencing within ten minutes after the launch and persisting for about four hours. The depletion extended over a region of approximately 1000-km radius. The observations were made in the course of routine Faraday-rotation measurements of the VHF signals from geostationary satellites ATS-3 and ATS-5.

Similar effects were predicted to occur with the Atlas-Centaur launch of satellite HEAO-C, which occurred at night on September 20, 1979.⁸ Because of the current practical interest in these phenomena as they relate to SPS environmental studies, an organized effort was mounted to obtain experimental observations, and a considerable body of data was collected. The data were reviewed in a DoE-sponsored workshop meeting held in Boston, November 11-13, 1979. Proceedings are to be published shortly.⁹ The observations included Faraday rotation polarimetry measurements of total electron content,^{9a-g} incoherent scatter radar measurements from Millstone Hill^{9h} and from Arecibo,⁹ⁱ differential Doppler measurements,^{9j} radio propagation measurements,^{9k-n} HF radar measurements,^{9o} and optical/IR airglow measurements.^{9p,q} We personally were involved in the airglow observations and the Arecibo observations, some of which are reported here. We also furnished prelaunch computer model predictions, which

we shall review in comparison with the post-launch data.

The ionospheric depletion effect of rocket exhaust gases, as first interpreted correctly by Mendillo et al,¹ is due to ion-molecule charge-exchange reactions, which enhance the effective rate of recombination of the existing F-layer ions and electrons. The essential point is that in the F2 layer (above 200-km altitude), the normal plasma consists of monatomic O^+ ions and electrons, and reactive molecules such as H_2O , H_2 , and CO_2 (or even O_2) are rare. When H_2O and H_2 are introduced, a sequence of reactions occurs that leads to the destruction of ions. The reactions also produce visible airglow, and they produce H atoms. The basic chemistry is as follows.

A. Chemical Reactions

The rocket exhaust molecules, predominantly H_2O and H_2 , undergo charge-exchange reactions with the O^+ ions, and the resulting molecular ions combine with electrons. With H_2O the sequence is



followed by



Reaction (2) is about 10^5 times faster than the direct recombination of electrons with O^+ , i.e.,



Reaction (1) is much faster than either of the normally occurring F-layer charge-transfer reactions



or



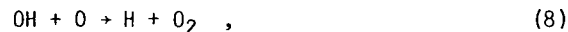
The OH radical formed in Reaction (2) can react further with O^+ . The reaction is



which is followed by rapid neutralization of the O_2^+ :



In most cases, however, the OH radical is destroyed by reaction with atomic oxygen, i.e.,



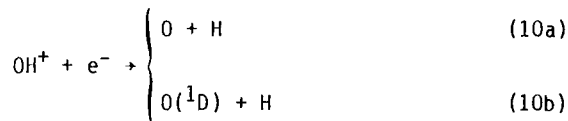
before Reactions (6) and (7) can occur to a significant extent.

The result of the two cycles, Reactions (1) and (2) and Reactions (8), (4), and (7) in sequence, is the destruction of between one and two electron-ion pairs by each H_2O molecule.

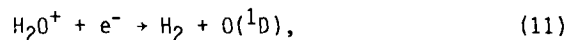
Similar processes occur with other common rocket-exhaust products, such as H_2 or CO_2 . With H_2 , the sequence is



followed by

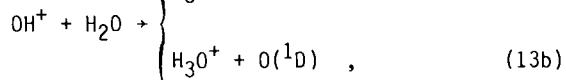
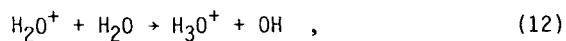


The $O(^1D)$ is a metastable, electronically excited oxygen atom that decays primarily by emission of 630.0-nm radiation. On the launch of HEAO-C, we obtained photometric data on the 630-nm airglow. For this reason, we will elaborate on the airglow chemistry. The $O(^1D)$ atoms produced in Reactions (7) and (10b) undergo radiative decay, with a lifetime of 120 seconds, and the resulting red-line emission can be observed from the ground. Some additional $O(^1D)$ atoms are probably formed in the reaction



which is a low-probability branch of Reaction (2). The branching ratios for $O(^1D)$ production in Reactions (2), (11) and (10) are unknown; however, they have been estimated theoretically by W. Wadt,¹⁰ as 5 and 10% respectively.

The water vapor emitted by a rocket is at quite high concentrations relative to the F-layer ions. For this reason, a number of reactions occur that compete with (2), (10), and (11). Some of these are



and



The branching ratio for $\text{O}(^1\text{D})$ production in Reaction (13) is unknown. However, on the basis of the HEAO-C airglow data, together with considerations of reaction energetics, we believe that it is near 100%.

B. Exhaust Gas Diffusion, Settling, and Transport

The severity, geographic extent, and duration of the F-layer depletions produced by the exhaust product molecules are determined by a combination of interacting processes including chemistry, diffusion, gravitational settling, and advection by prevailing winds. The molecular diffusion and settling rates are both rapidly increasing functions of altitude. For a quantitative description of these coupled processes, we built a two-dimensional computer model. Some numerical results from the model are detailed in the following sections. Details of the model itself are amplified in Sec. VI and Appendices A and B.

The strong ion-removal effects induced by exhaust product molecules are confined to the ionospheric F2 layer above 200 km, where the normally occurring ion species is predominantly monatomic O^+ . Below 180 km, the dominant ion species are polyatomic (principally NO^+ and O_2^+), and the effective rates of recombination of these ions with electrons are not affected much by the addition of contaminant molecules such as H_2O or H_2 . (In the E and F1 layers, the addition of H_2O should not lead to a drastic enhancement in the effective recombination rate. It might produce a

noticeable effect, nevertheless, by forming complex ions such as $\text{NO}^+ \cdot n\text{H}_2\text{O}$, H_3O^+ and $\text{H}_3\text{O}^+ \cdot n\text{H}_2\text{O}$. The recombination coefficients for these complexes are believed to be from 3 to 10 times larger than those of the normally occurring simple ions, NO^+ and O_2^+).

The fastest process affecting the removal of water molecules from the F-layer is gravitational settling (regulated, of course, by molecular collisions). The time required for an isolated water molecule to fall across the F-layer from 400- to 200-km altitude is about two hours. The settling and diffusion rates are computed in detail in the numerical model. The center-of-mass velocity of a gas cloud depends in detail on its vertical density profile. However, when the cloud is far from its final hydrostatic equilibrium distribution, a useful approximate value of the settling velocity is given by $\bar{w} \sim -(1/2)g/v$, where g is the acceleration due to gravity and v is the molecular collision frequency. For an H_2O cloud falling in an atomic oxygen atmosphere, the formula gives $\bar{w} \sim -5 \times 10^{12}/n$ m/s if n is the local number density in cm^{-3} . The hydrogen tends to settle also. However, its behavior is dominated by diffusion, and it diffuses away before it settles to a noticeable extent.

During their fall, the molecules diffuse laterally, and they react with O^+ ions. An isolated H_2O molecule falling across the daytime F-layer has a better-than-90% chance of reacting with an O^+ ion, if the O^+ concentration has not already been depleted by reactions with other H_2O or H_2 molecules. In most cases associated with large rocket exhausts, the descending H_2O cloud is dense enough to react with all the O^+ ions in its path. The concentration of molecules is overwhelmingly larger than the concentration of O^+ ions, so effectively all the ions are removed. The excess molecules fall through intact.

The diameter of the cloud increases with vertical distance fallen, and the cloud continues to spread after the settling has largely ceased. The H_2 cloud spreads about four times as fast as the water cloud, while its settling rate is about three times slower.

If, after destroying the existing ionization, the excess H_2O and H_2 settled completely out of

the F-layer, the ionization would soon return, due to the action of solar extreme ultraviolet radiation. In the daytime, the ion replenishment would take about two hours. However, the H_2O and H_2 would not settle out completely. Instead, they would maintain a quasi-steady concentration profile, falling off exponentially with altitude (z) approximately as $\exp[-(z - z_0)/H]$. Here z_0 is the altitude of maximum concentration and H is a scale height equal to about 50 km for H_2O and 400 km for H_2 . The base altitude z_0 descends with time, but at an ever-decreasing rate. After 8 hours, for H_2O , z_0 would be about 150 km, and after 24 hours it would be 120 km.

The H_2O and H_2 are gradually destroyed chemically, mainly by reactions with O^+ ions. The rate of destruction is essentially equal to the rate of production of ions by sunlight--a number of the order $10^3 \text{ cm}^{-3} \text{ s}^{-1}$ at 150- to 200-km altitude. With this small destruction rate, the molecules can survive for several days.

It is also notable that the reactions leading to destruction of H_2O and H_2 all lead invariably to production of H atoms (Reactions 2, 6, 8, 9, 10 and 14). Repeated HLLV launches will lead to production of very large quantities of H atoms, possibly enough to modify the upper thermosphere.

Dispersal of the exhaust products is hastened by the ionospheric winds. Typical wind speeds in the F-layer are 300 km h^{-1} , and they exhibit considerable shear.¹¹⁻¹⁶ This enhances the growth rate of the depleted region, but it also speeds up the recovery. Neutral winds in the ionosphere are believed to have a rather regular diurnal behavior. Therefore, to a limited extent, their effects may be regular and predictable.

The size and severity of the ionospheric depletion are influenced, of course, by the initial conditions of the problem, that is, by processes that occur early in time and determine the "initial" concentration and spatial distribution of the exhaust products. One such process is the condensation of water vapor to form ice crystals. Such condensation is to be expected on theoretical grounds,^{6,17} and it was observed to occur, in fact, during the translunar injection burn of Apollo 8 (Molander and Wolfhard¹⁸). A

similar ice cloud was observed in the Los Alamos-Sandia Lagopedo experiments (HE detonations in the F-layer).¹⁹ Under some circumstances, the condensation could have an influence on the rate of gravitational settling of the water. However, P. Bernhardt has shown²⁰ that the radii of water-cluster particles formed in typical exhausts are probably very small (ca. $.01 \mu\text{m}$), and the fractional condensation is also small. Therefore, the effect of condensation can probably be ignored.

The initial settling rates of the exhaust gases can also be influenced by "hydrodynamic" processes (as opposed to "diffusive"). That is, at early times when molecular concentrations of those gases are large (i.e., comparable with the background air), the falling gases impart substantial velocity to the air. When the air participates in the downward motion, it is less effective for slowing the descent. During that early stage, the falling velocities can be quite large, and it is important to understand the processes in some detail. These details are not included in our model. We attempt to simulate their effects by the way we set initial conditions for the numerical problem.

III. SKYLAB I LAUNCH

The first set of definitive data on an ionospheric depletion resulting from a rocket launch was obtained on the launch of Skylab I, as reported by Mendillo et al.^{1,2} One of the first tests for our two-dimensional model was to run a set of computations representing that specific case and to compare the computed results with the data.

We described these computations before,^{6,7} and the data were described and interpreted by Mendillo et al.^{1,2} The data consisted of a set of ionospheric electron column density (TEC) records, measured by Faraday rotation of VHF transmission from two communications satellites, ATS-3 and -5, from five different ground stations. All of the records showed a substantial reduction in electron column density commencing within a few minutes after the Skylab launch and persisting for about four hours. From the aggregate of the data, it was concluded that the ionospheric hole extended to a distance of 1000 km on either side of the launch trajectory plane.

All of our computer model simulations of the Skylab launch have shown that the TEC depletion should have persisted for much longer than four hours, and we attribute the observed four-hour duration to the effect of the ionospheric winds. The expected wind direction in the F2 region at the time of the launch would have been mainly southward, with a velocity sufficient to carry the hole out of the observational lines of sight in about the times observed.

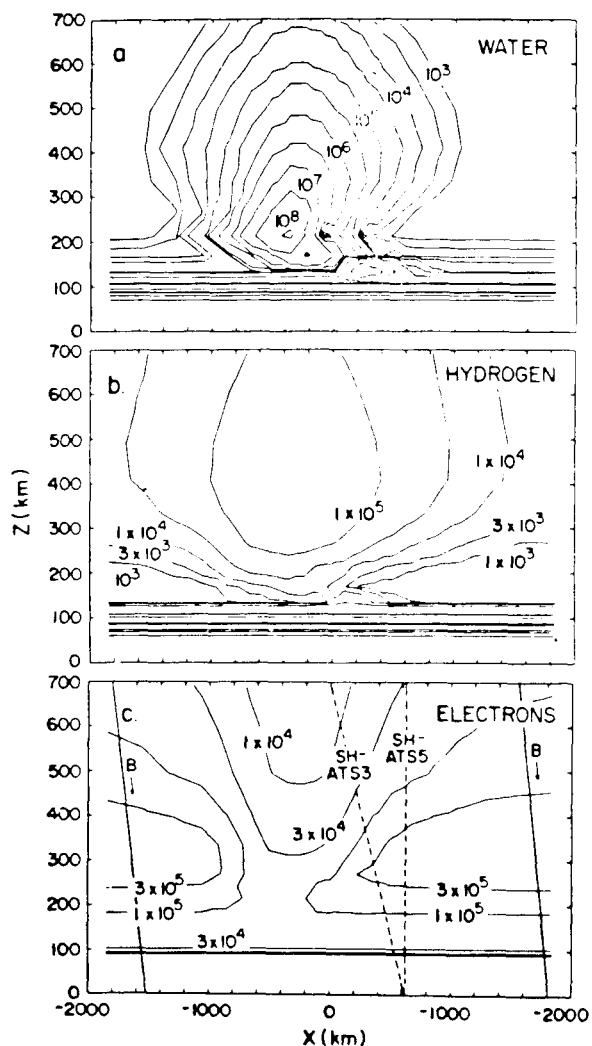


Fig. 1.

Computed concentration contours for H_2O , H_2 , and electrons (number per cubic centimeter) three hours after launch of Skylab. The (x, z) coordinates are in the magnetic meridian plane 1300-km downrange from the launch point, aligned at an angle of 70° from the launch plane. The cross-sectional view is looking backward along the trajectory. The original exhaust deposition was in the central plane $x = 0$. Also shown are the B-field direction and the observational lines-of-sight from Sagamore Hill to satellites ATS-3 and -5.

Figure 1 is a set of computed two-dimensional contour plots of H_2O , H_2 , and electron concentrations three hours after the Skylab launch. The view is in the magnetic meridian plane, which happens to be perpendicular to the launch plane. The trajectory was aligned in a north-easterly direction from Cape Canaveral, passing off the east coast of Newfoundland. We are looking southwestward along the launch trajectory. Two TEC observational lines of sight are shown, in addition to the B-field direction. The exhaust cloud and the electron hole, which originally were in the center, have blown to the left, away from the instrumental lines of sight. The computed width of the hole is in reasonable agreement with the observations, as is time-of-passage out of the lines of sight. The computation was continued until sunrise the next day, and the computed ionospheric hole persisted through the night.

Figures 2a and b are plots of total electron content vs time for the Sagamore Hill/ATS-3 line-of-sight. Figure 2a is the observational data on the Skylab launch day, taken from the paper by Mendillo et al.¹ Figure 2b is a plot of the computed TEC for the same line-of-sight for the 24

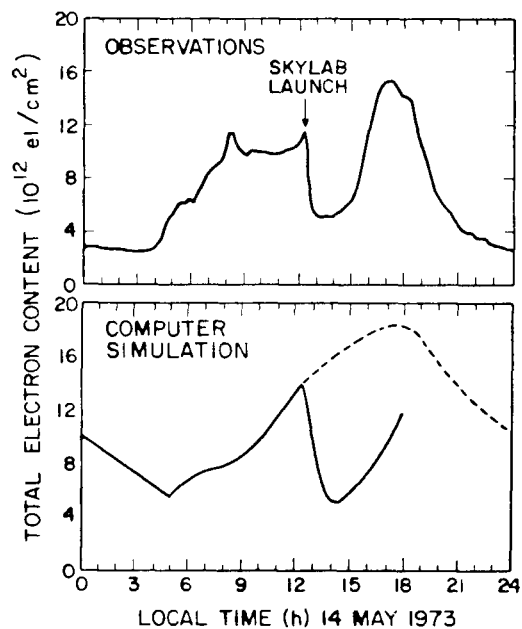


Fig. 2.

(a) Measured total electron content vs time following Skylab I launch on line-of-sight from Sagamore Hill Observatory to ATS-3 (Mendillo et al.^{1,2}). (b) Model computation of TEC vs time for the 24 hours preceding and 4 hours following the Skylab launch.

hours preceding and 6 hours following the Skylab launch. The qualitative features of the computed TEC-vs-time curve agree with the data. The same can be said for comparisons of the computed results with the data from the other lines of sight.

The model results depend critically on the thermospheric wind description used in the computations. We made a considerable effort to arrive at a reasonable model for the winds (see Appendix B). However, it is fair to ask what other evidence exists to support our belief that the dominant F-layer wind direction was southward, rather than some other direction. Some supporting evidence comes from the general character of the diurnal TEC variations observed during the month of May 1973, which are shown by Mendillo et al.¹ The steady increase in electron column density from morning through afternoon implies an F-layer wind system that is dominantly northward in the morning and southward in the afternoon, according to our computer model. Also, the similar character of the post-launch TEC records for the several different lines of sight¹ is further evidence of a southward wind.

IV. HEAO-C LAUNCH

The High-Energy Astrophysical Observatory Satellite HEAO-C was launched from Cape Canaveral at 0530 hrs GMT (0130 hrs local time) on September 20, 1979, aboard an Atlas-Centaur rocket. The launch trajectory, which was almost due eastward, was unusual in that the Centaur second-stage engines burned to an altitude of 501 km, depositing large quantities of exhaust gases directly into the F layer. It was anticipated by Mendillo et al.⁸ that an ionospheric hole would be formed, and a group of experimenters assembled (supported in part by the DoE SPS project) to make coordinated observations.

Figure 3 is a map showing the HEAO-C launch trajectory and locations of a few of the ground stations from which observations were made. Also shown are the ground traces of two polarimeter ray paths from Bermuda to the synchronous satellites ATS-3 and -5.

The collected experimental results, which are summarized in the Proceedings of the HEAO-C Workshop,⁹ held in November 1979, showed that a signi-

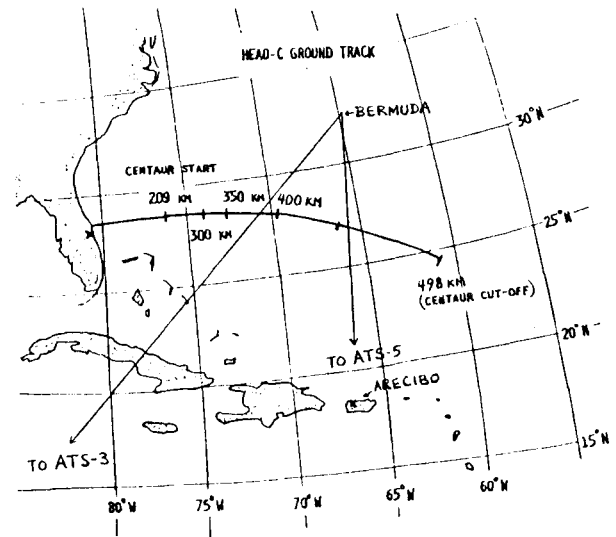


Fig. 3. Map showing the HEAO-C launch trajectory and a few observer locations and ray paths.

ficant F-layer depletion did occur over a region 600 to 800 km in north-south extent, and the depletion persisted until dawn.^{9a-r}

Our own participation consisted of (1) performing prelaunch computer model predictions of the morphology of the ionospheric hole; (2) performing incoherent scatter radar measurements of the ionosphere with the Arecibo radiotelescope; and (3) making optical airglow measurements from a ground station near Cape Canaveral.

We distributed our prelaunch computer model predictions to the set of announced HEAO-C participants. The predictions included computed vertical profiles of composition of the prelaunch ionosphere, and contours of concentrations of electrons, $O(^1D)$ atoms, and H_2O and H_2 molecules at times of one and three hours after the launch. The post-launch analysis of experimental data showed that our predictions were borne out in some but not all details. We predicted a 1000- to 1500-km diameter region of severely depleted ionization, persisting until dawn, somewhat as observed.^{9a-h} However, the computed airglow intensity was less than the observed,^{9i,n} and the computed north-south extent was larger than the observed. The prelaunch set of computed contours of H_2 , H_2O , and electron concentrations three hours after launch is shown in Fig. 4. The contours represent a vertical north-south cross section of the rocket trajectory, 1100-km downrange.

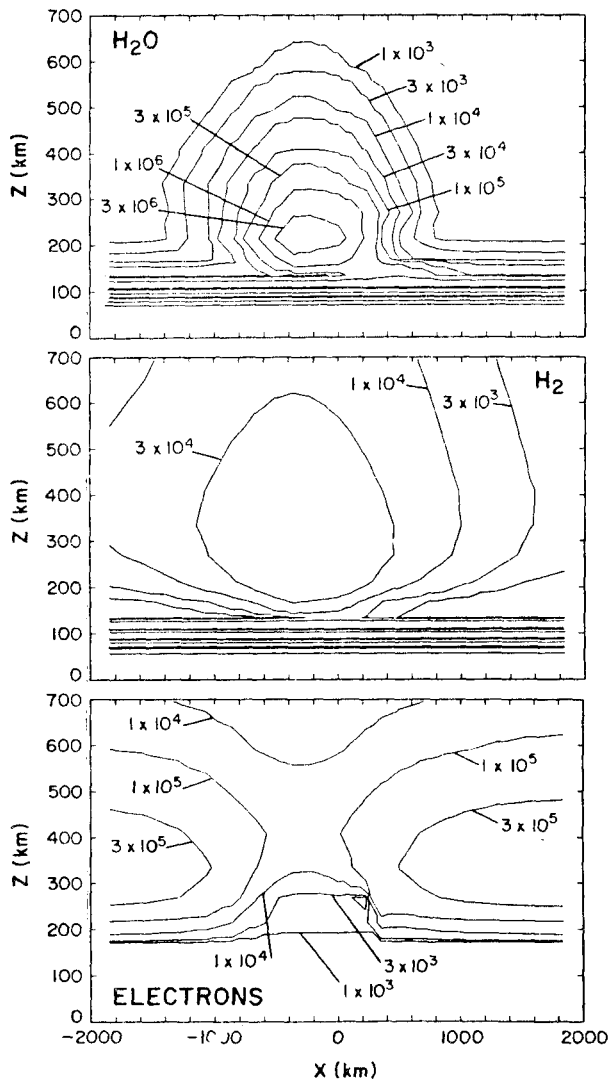


Fig. 4.

Computed contours of concentrations (cm^{-3}) of H_2O , H_2 , and electrons three hours after Atlas Centaur launch. The view is a cross section in the Arecibo magnetic meridian plane. Magnetic south is to the left (prelaunch predictions).

A. Arecibo Observations

The Arecibo incoherent-scatter radar measurements were performed by L. M. Duncan and R. Behnke. The 430-MHz radar was programmed to scan back and forth from north to south via west at a fixed zenith angle of 15° , with periodic 15-minute holds in the northward and southward directions. The complete cycle required 70 minutes, and was carried out repetitively.

To provide baseline data, an identical schedule of measurements was carried out from 11 pm to 7 am local time on the night preceding and two

nights following the HEAO-C launch, in addition to the launch night itself.

Graphical presentations of the computer-processed data include contours of electron density as functions of time and altitude along the changing antenna line-of-sight. A presentation of this sort for the HEAO-C launch night is shown in Fig. 5a. A plot of maximum electron density vs time at the F2 peak is in Fig. 5b.

It was found that the ionosphere was quite variable from night to night, as is characteristic of equinox periods. The characteristic "midnight collapse" was evident each night, with the F2 maximum decreasing both in altitude and peak electron density over a period commencing between about 1 and 3 am local time and continuing until dawn. The precise timing and strength of the midnight collapse was variable.

Earlier Arecibo data had led us to expect that the most likely direction of the thermospheric winds at HEAO-C launch time would be southward, so that the Centaur exhaust cloud would be carried southward toward the radar (the Arecibo-to-launch-plane distance was 1100 km). However, the observed behavior of the ionosphere on the four days of measurement indicated that the winds were probably shifting to northward between 1 and 3 am local time.

On the night of the HEAO-C launch, a particularly strong midnight collapse phase began at about 1:15 am local time--i.e., about fifteen minutes prior to the launch (see Fig. 5b). The process of collapse was observed to propagate from south to north, indicative of a northward-shifting wind. Between 1100 pm and 0115 am, the F2 peak dropped steadily in altitude from 360 to 275 km, while maintaining a relatively constant peak electron density of $2.5 \times 10^6 \text{ cm}^{-3}$. Between 0115 and 0130, the peak altitude dropped more rapidly to 260 km, and the electron density began decreasing, dropping to $2.0 \times 10^6 \text{ cm}^{-3}$ by 0145, to 1.5×10^6 by 0200, and continuing to decrease gradually to a predawn minimum value of $4 \times 10^5 \text{ cm}^{-3}$ at 0600. Nothing in this behavior was particularly unusual, and nothing could be uniquely attributed to the HEAO-C launch. Surprisingly, no anomalous effect was seen even in the topside ionosphere above 1500 km, even though that region was in direct

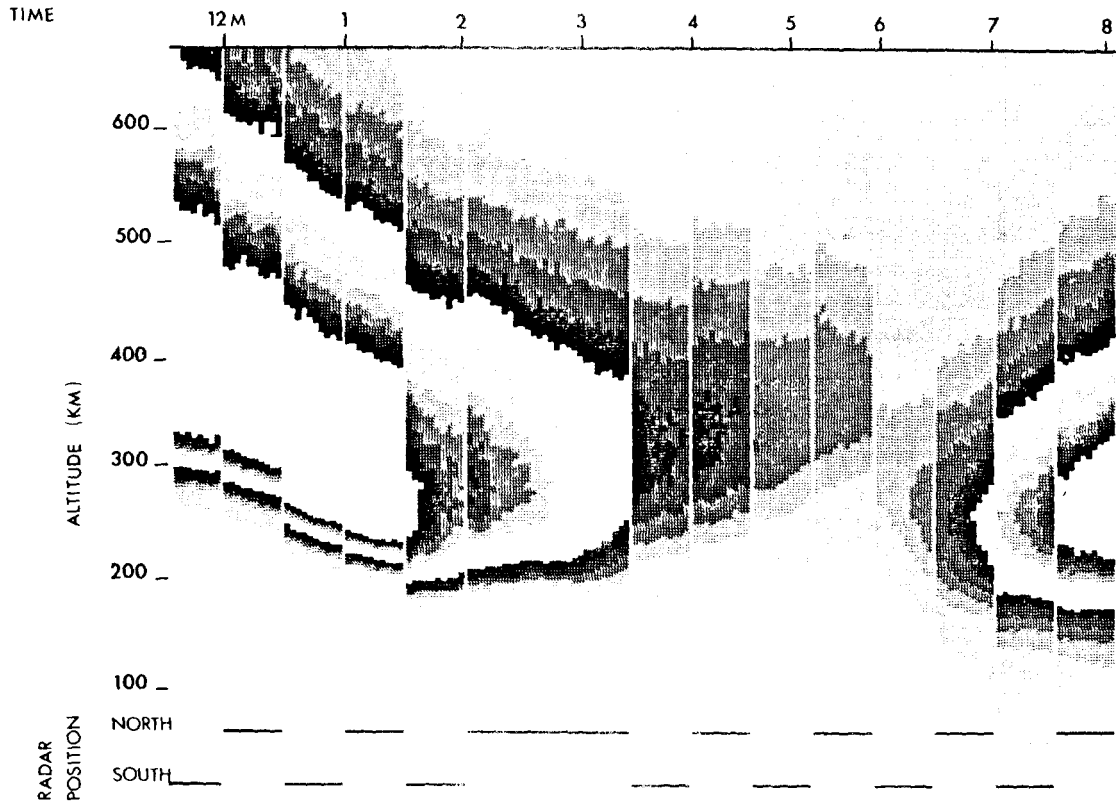


Fig. 5a.

Shaded contour plot of electron density in the ionosphere for 19-20 September, 1979. Two octaves of shades are shown, with darker shades corresponding to greater densities, in steps of 10^5 electrons/cm³. The intermediate white level represents an absolute density of 10^6 electrons/cm³. Only data taken at the north and south fixed radar positions are presented.

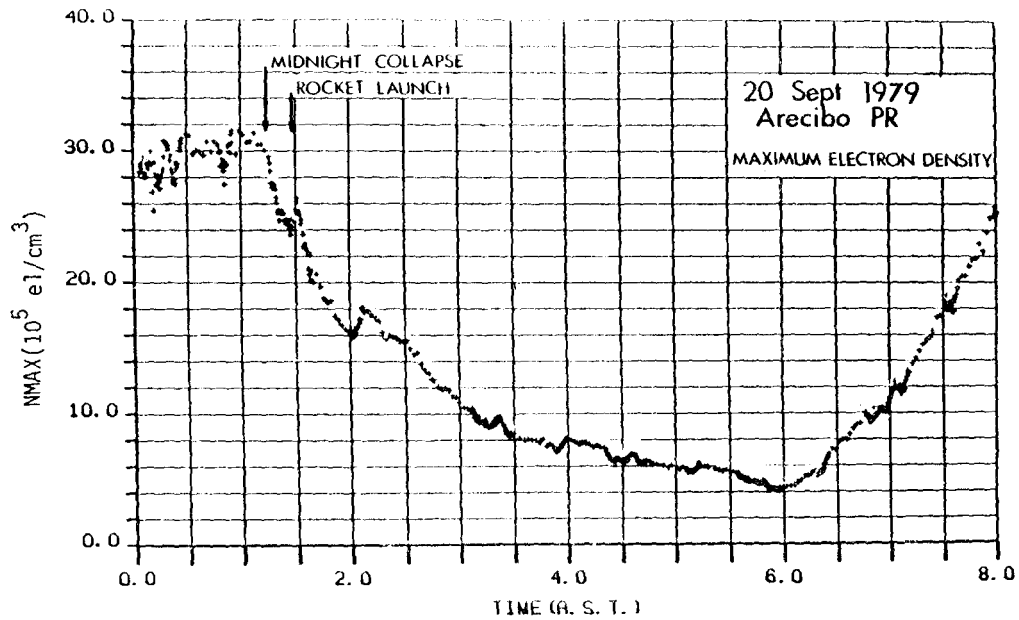


Fig. 5b.

Arecibo 430-MHz incoherent-scatter measurements of F2 peak electron density.

communication with the launch trajectory along magnetic field lines.

We conclude that a northward-blowing F-layer wind system at HEAO-C launch time prevented the ionospheric hole from spreading into the Arecibo radar line-of-sight. Other data, primarily the TEC data from Florida, Georgia, and Bermuda, indicated that a hole did indeed form, and that it had a north-south width of roughly 600 km.^{9b,9,i} Thus, the absence of a southward wind was sufficient to explain the fact that the main F-layer depletion did not reach Arecibo. It is more surprising that no effect was detectable in the topside ionosphere. The observation suggests that electric fields may have been set up that caused the hole to fill in at the top.

B. Optical Observations

Through the courtesy of the Air Force and SAMS0, we obtained permission to set up an optical field station at the Malabar tracking facility near Melbourne, FL. Our equipment included a scanning spectrometer, a photometer, a 35-mm camera and tripods, recorders, and accessories.

The photometer was operated with a narrow-band 630-nm interference filter, and the output was fed to a pen recorder. The photometer-filter combination had been calibrated in the laboratory against a standard tungsten lamp source. The instrument had a 3° angular field of view, and was pointed manually. The 35-mm camera was coaligned with the instrument. Its primary purpose was to record star images for later checks on the pointing. Our selection of pointing directions was based on prelaunch computations of the vector directions to the ascending rocket as functions of time.

The spectrometer detector was a S-20 photomultiplier with thermoelectric cooler. The output was fed to a second pen recorder. At the time of the launch, there were broken clouds, which did not seriously hinder our observations. There was no moon.

The photometer provided excellent data. We obtained a continuous two-hour prelaunch record of the 630-nm night-sky background emission and a detailed record of the enhanced post-launch airglow produced by the chemical reactions of exhaust

molecules with the ionosphere [see Reactions (7), (10), (11), and (13)]. The night-sky background intensity along the instrumental line of sight (ca 20° elevation angle), after correction for atmospheric transmission (correction estimated, equivalent to 0.76 at zenith), increased gradually from 292 to 360 Rayleighs during the two-hour period before launch. At six minutes after launch, the intensity rose sharply, reaching a peak level of 20 kilorayleighs at nine minutes. Then it decreased gradually for the next two hours, with an e-folding time of about fifteen minutes. A plot of the measured intensity vs time is shown in Fig. 6.

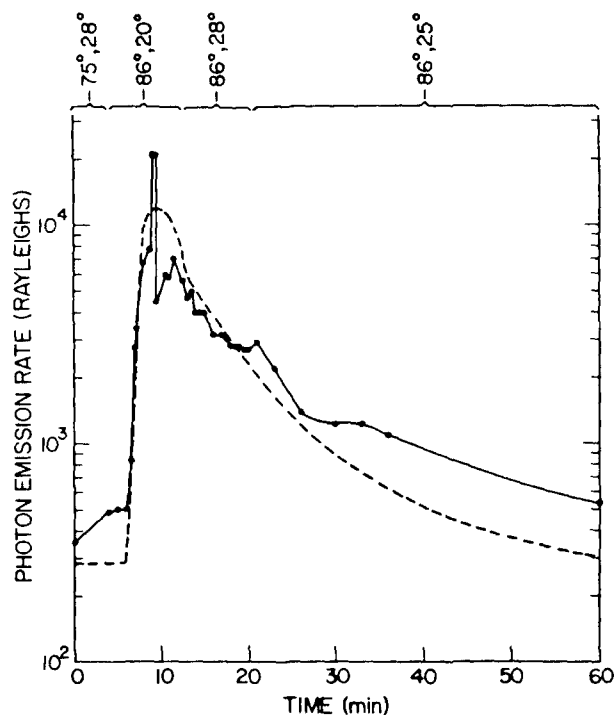


Fig. 6.
Solid curve: 6300-Å photometer data from Malabar, FL, corrected for atmospheric transmission. Pointing directions (azimuth, elevation) are indicated at top of figure. The dashed curve is the model computation of 6300-Å airglow for the same lines of sight.

The scanning spectrometer proved to be less sensitive than we had expected. We were unable to detect any natural night-sky line or band emissions prior to the launch. At launch time we commenced a schedule of repeated five-minute scans over the wavelength range 620 to 670 nm. At 8.5

minutes we detected a strong emission line at 630 nm, along with its weaker partner at 6364 Å. No other lines or bands were seen. At 15 minutes we again detected the 630-nm line, though very weakly.

The 35-mm camera (with 50-mm lens) was operated with tri-x film and without filter. It recorded star images as intended, using 1.5- to 2-minute exposure times. To our surprise, it also recorded several spatially-resolved photographs of the airglow. The first frame, recorded before the rocket entered the F layer, shows a weak trace of the rocket trajectory.

Before development, the tail of the 35-mm film was exposed in a photographic sensitometer with a step wedge. This permitted the measured densities on the film to be interpreted in terms of source radiance. After development, several of the frames were scanned with an automated densitometer, and the data were processed by computer to generate values of net density and/or source intensity (with the prelaunch background subtracted) vs position in the photograph. The image processing algorithm also deleted the stars. The processed data of net film density vs position can be presented by the computer in the form of synthetic photographs, which are enhanced representations of the original photographs. The first two image-enhanced photographs of the Atlas Centaur airglow are shown in Figs. 7a and b. The photograph for Fig. 7a was exposed at 8.3 to 10.1 minutes after launch; that of Fig. 7b was exposed at 10.7 to 12.5 minutes.

The horizontal extent of the airglow region, as deduced from the image in Fig. 7a, was 420 km (1500-km distance assumed; $t \sim 9$ minutes). From Fig. 7b, the horizontal extent was about 700 km (2000-km distance assumed; $t \sim 12$ minutes). The measured total sky background intensity, as deduced from a prelaunch photo, was equivalent to 21 kilorayleighs at 630 nm (assuming 33% optical transmission). The peak intensity in frame 6a was 17 kilorayleighs above the background, in agreement with the photometer measurement. The peak intensity in frame 6b was 13 kilorayleighs above background.

These airglow measurements compare rather well with those of I. Kofsky,⁹ⁱ which were made

from an aircraft flying under the HEAO-C launch trajectory. Kofsky's measurements at 630 nm gave a peak zenith-radiance of 8 kilorayleighs at ten minutes after launch, in excellent agreement with our peak measurement of 20 kR on a line of sight aligned with the launch trajectory at an elevation angle of 20° . His observation of a north-south width of about 600 km is also in good agreement with our results.

The fact that the airglow did not appear until six minutes after the launch, when the rocket was at 300-km altitude, is consistent with our prelaunch expectation that the bottom of the F layer was at 300 km. It is, however, not consistent with the Arecibo measurement, which showed the F-layer peak to be at 260 km. The ionosphere over Arecibo was evidently quite different from the ionosphere east of Florida.

C. Polarimeter Measurements of TEC

In the computer model discussion, we will make use of the Bermuda Faraday rotation (total electron content) data, which have been described by Reilly^{9e} and other TEC measurements from the Florida peninsula, described by Baumgardner et al,^{9a} Bernhardt et al,^{9b} Goodman et al,^{9c,d} Soicher and Gorman,^{9f} Mendillo and Bernhardt,^{9g} and Clynch.^{9h}

Two polarimeters, operated by the US Naval Research Laboratory, were located on Bermuda, and measured the Faraday rotation of VHF signals from the geosynchronous satellites ATS-3 and -5. Ground traces of the ray paths are shown in Fig. 3. The ATS-3 ray path passed above the rocket trajectory at a distance of 49 km; the ATS-5 ray path passed above the trajectory at a distance of 221 km.

Data were recorded continuously over the period September 17 through 23, and they were calibrated against similar data recorded at Patrick AFB, FL. Figure 8, from Reilly,^{9e} shows the Patrick AFB TEC data for the three consecutive prelaunch days, September 17 to 19, and a computed TEC-vs-time plot, which will be explained in the next section.

On the launch night, both the Bermuda ATS-3 and -5 TEC records showed a sudden and pronounced drop within one minute of the times of closest approach of the rocket to the respective ray paths (Fig. 9). In fact, as noted by Reilly, the ATS-5

1 minus B smoothed

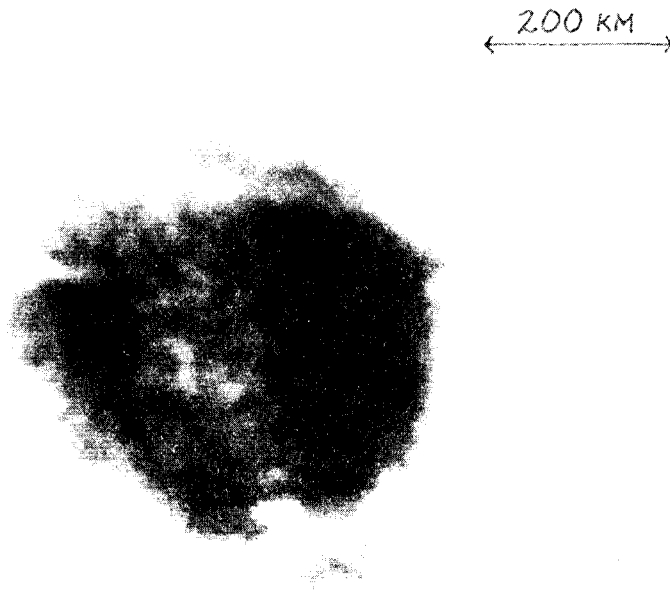


Fig. 7a.

An image-enhanced photograph of airglow produced by the HEAO-C launch, as seen from Malabar, FL, at nine minutes (exposure from 8.3 to 10.1 minutes) after launch. The background has been subtracted by the computer.

2 minus B smoothed

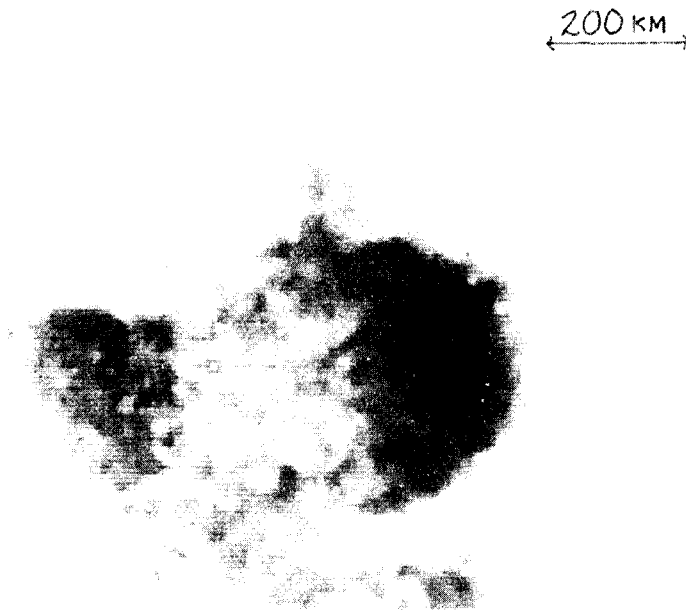


Fig. 7b.

An image-enhanced photograph of airglow produced by the HEAO-C launch, as seen from Malabar, FL, at nine minutes (exposure from 10.7 to 12.5 minutes) after launch. The background has been subtracted by the computer.

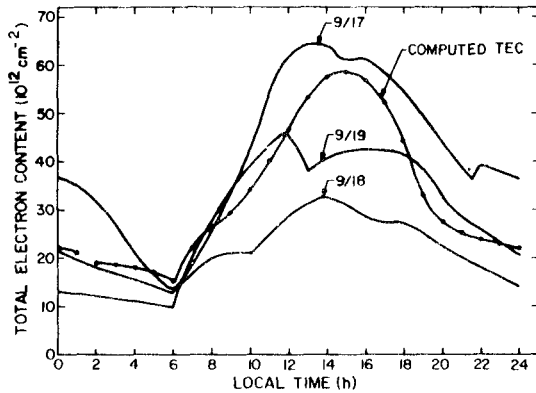


Fig. 8.
Vertical electron column density (TEC) as measured from Patrick AFB, FL, on September 17, 18, and 19. Also shown is the computed TEC, as generated by the model.

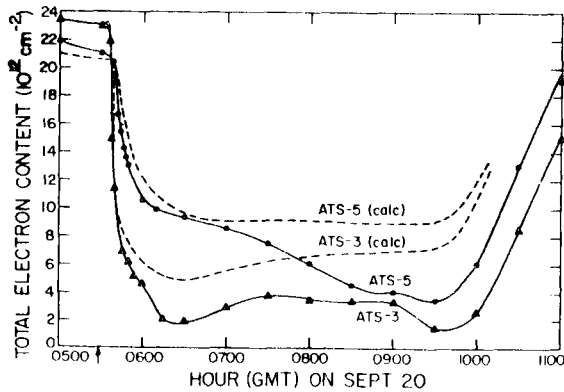


Fig. 9.
Comparison of the computed and measured TEC for the two observational ray paths of the Bermuda polarimeters to satellites ATS-3 and -5, respectively, for 30 minutes preceding and 5-1/2 hours following the HEAO-C launch.

TEC curve began to drop about four minutes before closest approach. (This may be related to the strong midnight collapse observed at Arecibo.) Both the ATS-3 and -5 records showed a large persistent TEC depression lasting until dawn.

A number of other Faraday rotation measurements were made from the Florida peninsula and Georgia, using VHF transmissions from the Italian satellite Sirio.^{9a,b} The ray paths were aligned mostly east-west, and concentrated along the axis and southern boundary of the ionospheric hole. From the aggregate of the data, it was concluded (Mendillo and Bernhardt^{9g}) that the north-south width of the hole was about 600 km, and that the hole moved gradually northward.

D. Post-Launch Analysis and Computations

Upon comparing the experimental data with our prelaunch computations, it is evident that

1. The ionospheric winds did not blow southward as strongly as we had assumed, and may have switched to northward. The hole did not blow over Arecibo.
2. The prelaunch F-layer peak electron density over Arecibo was larger than our model predicted, and the peak was at a lower altitude. However, the time of commencement of 6300-Å airglow suggested that the F layer at Cape Canaveral latitude was above 300 km, more like our predictions. The drop in h_{max} and the associated midnight collapse appeared to be a propagating process moving from south to north.
3. A substantial ionospheric hole did form and did persist until dawn, as predicted, but the size was smaller than we predicted.
4. The 6300-Å $O(^1D)$ airglow intensity, as measured from Malabar site 30 minutes after launch, was 1066 Rayleighs above the night-sky background. The prelaunch-computed 6300-Å intensity for the same time and elevation angle was 724 R -- about 30% less than the observed. Because of the way that we specified the initial conditions, the computation was not set up for application to times earlier than 15 minutes after launch. Therefore, we did not have predictions for the early period when the airglow intensity was maximum.
5. As noted by Reilly,^{9e} the commencement of TEC dropouts, as measured by the polarimeters on Bermuda, were remarkably early and sudden. Particularly surprising was the speed of the dropout on the Bermuda-ATS-5 ray path, which was 221 km from the rocket trajectory at the point of closest approach. In fact, the TEC decrease was observed to begin three minutes before the rocket reached the closest point to the ray path, and to continue thereafter with an e-folding time of about 12 minutes.

We have had difficulty understanding the ATS-5 results in view of the low concentration

that the H_2 molecules would have had at the distance of 221 km from the trajectory and the slowness of the $H_2 + O^+$ reaction [Eq. (9)]. It is unlikely that the concentration of H_2 molecules could have ever exceeded $3 \times 10^5 \text{ cm}^{-3}$ on the Bermuda-ATS-5 ray path. Then if the rate constant for Reaction 9 is $2 \times 10^{-9} \text{ cm}^3/\text{s}$, the published value, the e-folding time for O^+ removal could not have been shorter than 28 minutes. The H_2O molecules could not have affected the results until 4 minutes after the rocket passage, because of the small molecular velocity of H_2O , relative to H_2 .

The early expansion of the rocket exhaust above 350 km cannot be treated with diffusion theory (or the diffusion-like algorithms used in our computer model), because the collision mean-free paths are too long. The expansion is more nearly ballistic; i.e., the molecules expand freely, while falling under gravity. We have used a ballistic model for starting the HEAO-C computer simulations. The ballistic model leads to a faster-expanding, flatter radial distribution of molecules at large distances from the trajectory. Even so, we still cannot account in detail for the Bermuda-ATS-5 TEC results at times earlier than 15 minutes after launch. The discrepancy would largely disappear if we were permitted to assume that the effective rate coefficient for Reaction (9) is twice as large as the published value.

Since the time of the HEAO-C launch, we have been refining the computer model in the hope of producing a better match to the assembled data. We improved the mathematical algorithms with which we compute the plasma motion (see Appendix B). We added algorithms to compute the individual species' collision frequencies and diffusion coefficients in more detail. We expanded the chemistry to include He^+ and metastable $O^+(^2D)$ ions, and we added the second [$O(^1D)$] branch in Reaction (13). We also improved the thermospheric temperature model and photoionization rate computation to reflect changes due to changing solar activity. We refined our model for the initial ballistic transport of the rocket exhaust products and made the mesh size finer, so the code would give a better representation of the early development of the hole and the airglow.

The new plasma diffusion algorithms lead to larger F2 peak plasma densities, more like those that we measured at Arecibo. The larger plasma densities lead to more rapid chemical reaction with the rocket exhaust gases, and more intense airglow. The improved diffusion coefficients lead to slower radial growth of the H_2 and H_2O clouds and to a smaller ionospheric hole.

Since there was no evidence of a southward-blowing neutral wind at HEAO-C launch time, we modified the wind model for a new HEAO-C model computation so that the normal night-time southward wind was turned off at 1 am. This caused a rapid 30-km drop in the F2 peak altitude. At 0138 EDT, the rocket exhaust products were added, with a spatial distribution described by the ballistic trajectory model 100 seconds after release.

Some of the computed results are shown in Figs. 6 and 8 through 12. Figures 10a and b show sets of computed vertical concentration profiles for neutral and ionized species, respectively, at 0128 EDT, just before the launch. Figure 8 shows computed total electron content for the 24 hours preceding the launch, plotted together with the Patrick Air Force Base TEC measurements over the three days preceding the launch. The data indicate an ionospheric disturbance on September 18, which apparently recovered on September 19.

Figure 11 shows sets of computed two-dimensional contours of the concentrations of H_2 , H_2O , and electrons one hour after launch, 1500 km downrange from the launch site (trajectory altitude, 450 km). Also shown are approximate projections of the lines of sight for the two polarimeters on Bermuda to satellites ATS-3 and -5, respectively. Figure 9 is a composite plot of the computed TEC for the two polarimeter lines of sight, together with the experimental data. With respect to the amount and duration of the TEC reduction, as well as the east-west extent of the hole, the new computations are in good agreement with the data. They are much better than the prelaunch computations.

Figures 12a, b, and c show computed contours of $O(^1D)$ concentrations at 11, 14, and 18 minutes after launch, respectively. The 6300-Å airglow intensity in Rayleighs should be 8.3×10^{-9} times the $O(^1D)$ column density. The computed 6300-Å

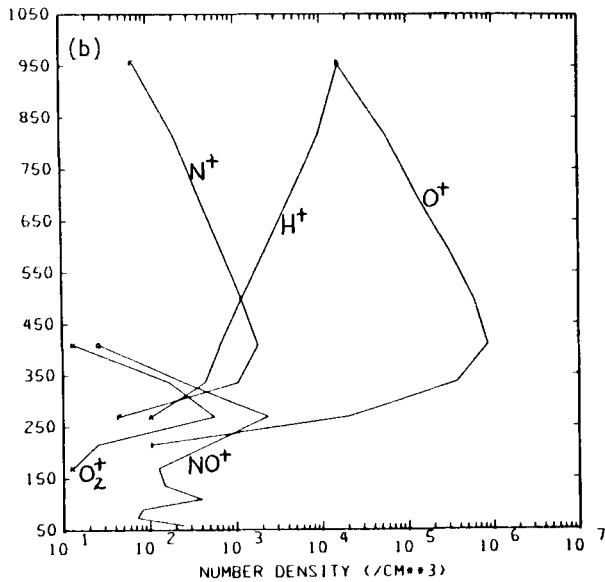
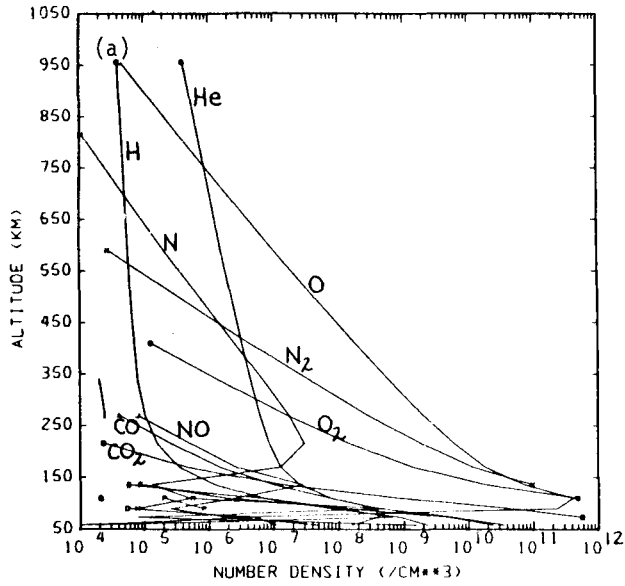


Fig. 10.

Computed vertical concentration profiles for neutral species and positive ion species respectively at 0530 GMT on September 20 at Cape Canaveral, FL--input conditions for setup of HEAO-C launch computation.

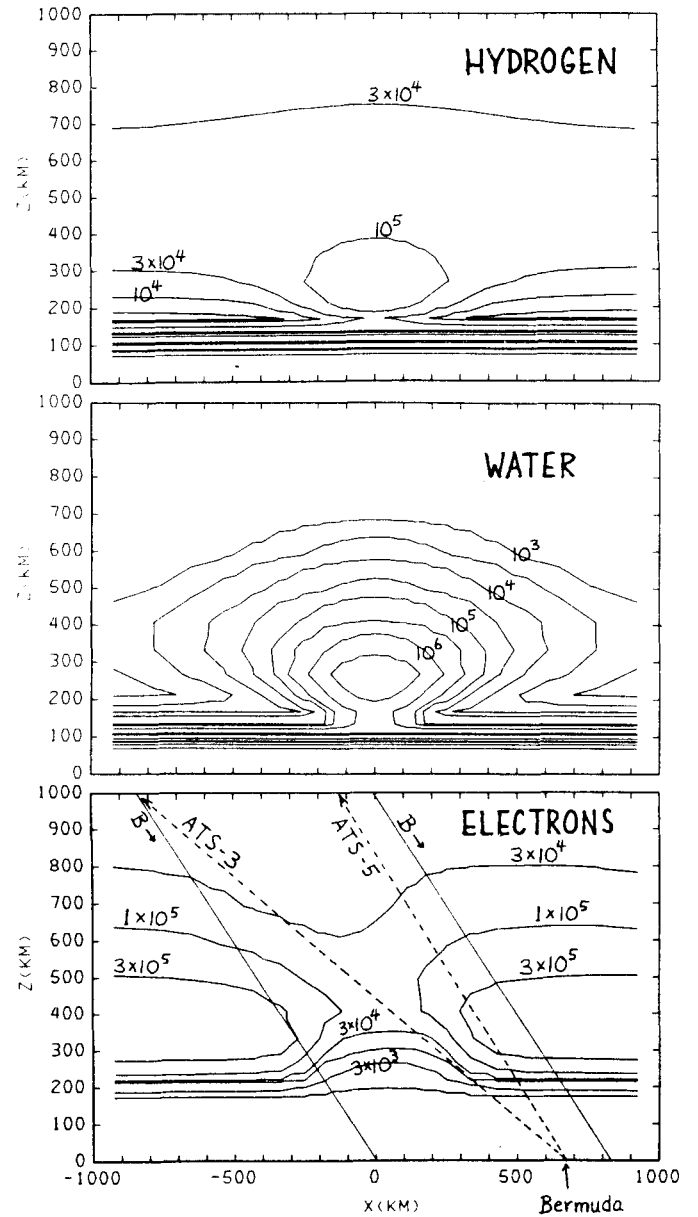


Fig. 11.

Computed contours of H_2 , H_2O , and electron concentrations (number per cubic centimeter) one hour after the HEAO-C launch. The (x,z) coordinates are in the magnetic meridian plane 1500-km downrange from the launch point, looking back along the trajectory. Also shown are the B-field direction and projections of the lines of sight of the two Bermuda polarimeters.

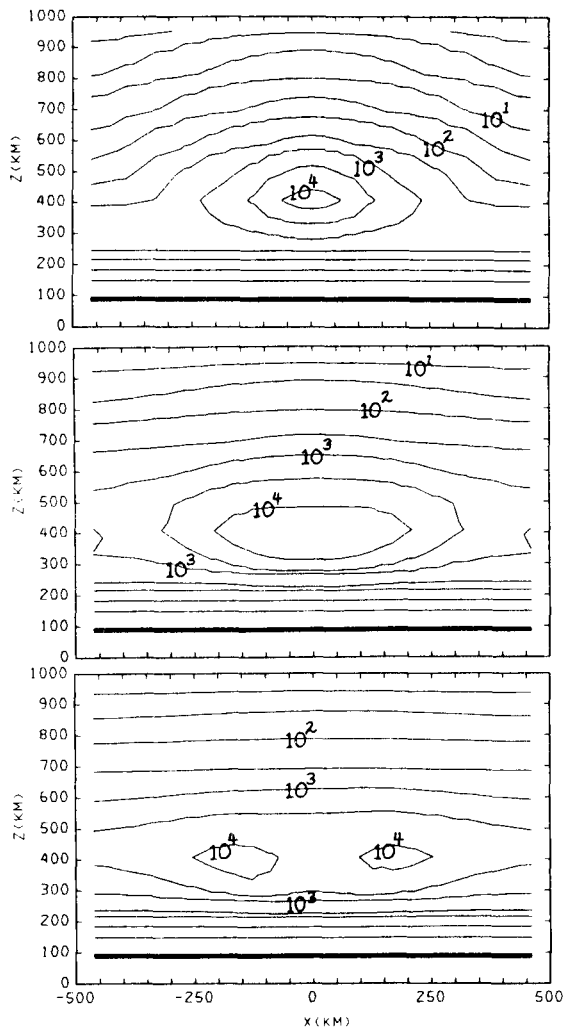


Fig. 12.
Computed contours of $O(^1D)$ concentrations 1500-km downrange from HEAO-C launch at 11, 14, and 18 minutes after launch.

airglow intensities for the line of sight from Malabar are plotted as the dashed curve in Fig. 5, for comparison with the data. The agreement is not bad. Also, the crosswise dimensions of the computed $O(^1D)$ contours in Fig. 12 agree well with the enhanced photographs from Malabar, shown in Figs. 7a and b.

V. HLLV COMPUTATIONS

Based on the quality of agreement between the computer model simulations and the experimental data from the Skylab and HEAO-C launches, we are cautiously optimistic that we can predict some of the F-layer effects of an HLLV launch. In this

section we describe computations of two phases of a hypothetical HLLV flight profile.

A. HLLV Second-Stage Burn at 56- to 124-km Altitude

The current Solar Power Satellite HLLV launch scenario, designed to minimize F-layer problems, calls for burning the second-stage engines only up through 124-km altitude. This leads to an eccentric initial orbit, which is later circularized by a brief burn near the apogee point at 477 km.

With respect to F-layer depletion problems, this launch scenario is definitely preferable to the "direct insertion" alternative where the second-stage engines are burned all the way to the circular-orbit altitude. The ion chemistry in the 56- to 124-km altitude range (D and E layers) is very different from that which occurs in the F-layer. The normally occurring ion species are NO^+ and O_2^+ instead of O^+ . These ions rapidly recombine with electrons, but they are continually replenished in the daytime by solar photoionization. At night they largely disappear. Addition of water vapor or H_2 does not have a very drastic effect on these processes.

Diffusion and gravitational settling are both much slower at these altitudes than they are in the F-layer. Horizontal spreading of the exhaust products would be caused primarily by fluctuating horizontal wind shears, and might amount to 1000 km per day. (The estimate of 1000 km per day for the spreading of exhaust products in the altitude range 56 to 125 km is based on theoretical estimates of the vertical shear of the tidal wind, from Garrett and Forbes.¹⁴ A typical value is 1 m/s/km, or a velocity difference of 50 m/s over 50 km. A velocity difference of 50 m/s, if extended over a 24-hour period, would lead to a lateral displacement of 4000 km. The shear would actually vary in an irregular but quasi-periodic fashion. These numbers suggest that 1000 km is a reasonable order-of-magnitude estimate of the net daily dispersion). A gradual upward diffusion would also occur, bringing some H_2 and H_2O molecules into the F-layer in the course of one or two days.

We ran a computation that represents a portion of the HLLV second-stage burn trajectory, covering a ground distance of 300 km and an altitude range between 118 and 123 km, with deposition

of 2.54×10^{31} molecules of H_2O and 8.5×10^{30} molecules of H_2 . The launch was assumed to occur at Cape Canaveral at noon.

The computed results showed, as expected, that exhaust-cloud diffusion and settling rates are quite slow. In the course of 24 hours, some water and H_2 does diffuse up to the F2 layer, where it reacts with O^+ ions. Because the molecular diffusion rate is very slow, the O^+ ions are replaced by solar photoionization about as fast as they are destroyed. At the same time, the H_2O and H_2 molecules are destroyed as fast as they diffuse into the F2 layer. Although the O^+ ions are replaced rapidly, the reaction sequence leads to a net production of H atoms. The H atoms are not destroyed, and they may accumulate in the upper thermosphere.

Figures 13a, b, and c include sets of contours of H_2O , H_2 , and electron concentrations at noon, 24 hours after the launch. They show that the H_2O and H_2 molecules are destroyed almost as fast as they diffuse into the F2 region, and, in the daytime, the electrons are replaced as fast as they are removed. At night the electrons are not replaced, and their concentration at the F2 peak is decreased to about 70% of the normal value.

It is possible that the H atom production could be a significant environmental problem. Its net effect could be to increase the density of the upper thermosphere. Within the first 30 hours after the HLLV launch, 1.3×10^{31} H atoms are produced above 100-km altitude from the added H_2O and H_2 . This can be compared with the normal global inventory of H atoms above 100 km, which is of the order of 4×10^{32} , and it implies that each HLLV launch could increase the thermospheric H inventory by about 3% per day if other sources and loss rates remained unchanged. From each launch the H production would continue for about five days, leading to a maximum upper limit global H atom inventory change of about 15%. However, an increase of thermospheric H-atom concentration would probably lead to an increased exospheric escape rate. The consensus of a number of studies on the global H-atom escape rate gives a value of about 1×10^{32} atoms per day. Thus, the normal thermospheric residence time for an H atom is of the order of four days (or perhaps one to ten days).

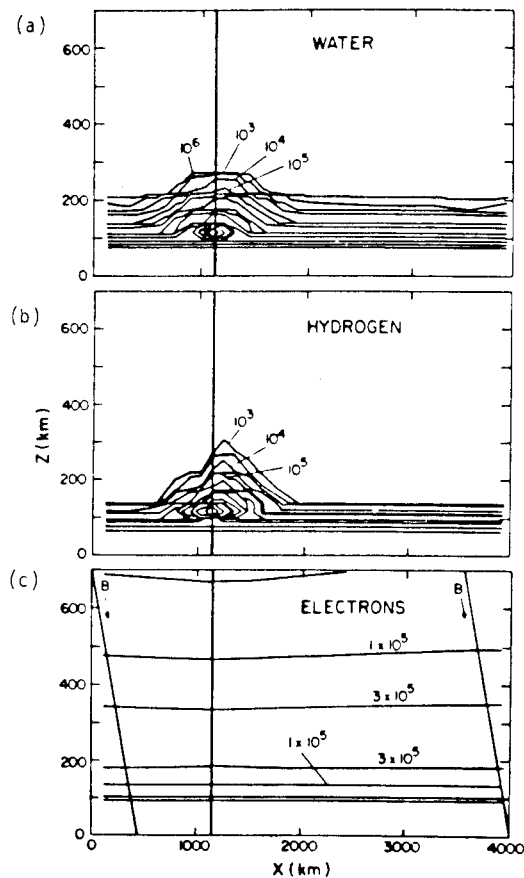


Fig. 13. Computed concentration contours for H_2O , H_2 , and electrons (number per cubic centimeter) 24 hours after hypothetical HLLV launch, which was assumed to occur at Cape Canaveral at noon on May 14. The view is perpendicular to the launch plane looking west.

The subject of thermospheric H-atom inventories and escape rates needs to be studied more carefully. The present calculations suggest that a doubling of the upper thermospheric density might be possible if a schedule of frequent HLLV launches were initiated. The possible consequences of a density doubling could be serious, though presently a matter of vague speculation. Thermospheric wind patterns could be affected, as well as relativistic electron precipitation rates and global climate.

The HLLV would also deposit large quantities of water vapor in the mesosphere. At the mesopause (~85-km altitude), the normal temperature is about 180K, and the saturation concentration of

water vapor in equilibrium with ice at that temperature is 2×10^{12} molecules/cm³. According to the design rate of output of water vapor in the HLLV exhaust ($4. \times 10^{29}$ molecules per linear kilometer), we would expect a large contrail to form at 85-km altitude with crosswise dimensions of at least 14 km. A contrail of this size would persist for at least several hours. [At the normal mesopause temperature of ca 180K, the saturation vapor pressure of water would be .05 d/cm², corresponding to an H₂O number density of 2×10^{12} molec/cm³. The normally existing H₂O concentration at the mesopause is less than a thousandth of this value. The HLLV, in its flight across this region, would emit about 4×10^{24} H₂O molecules per linear centimeter, resulting in local H₂O concentrations that would exceed saturation for some period of time. The length of time required for the concentration to drop below the 2×10^{12} molec/cm³ saturation level would be determined by wind shears and turbulent diffusion. Effective diffusion coefficients in this altitude regime, determined from radio meteor and chemical release data, vary between 10^6 and 10^7 cm²/s, see Zimmerman and Murphy,²¹ leading to supersaturation lifetimes of the contrail ranging between five hours and two days.]

A cumulative effect is possible over the course of many HLLV launches. The photochemical lifetime of H₂O vapor at 85 km is about 36 days. The presence of abnormally high H₂O concentrations can lead to an abnormally low mesopause temperature and to an increased likelihood of persistent condensation, i.e., mesospheric ice clouds. The sequence of events is complex, but roughly as follows.

The main source of radiative heating at 80 to 90 km is absorption of sunlight by ozone. An equivalent amount of radiative cooling comes from long-wavelength infrared (LWIR) emission by CO₂ and water and infrared chemiluminescent emission by OH. An increase in water concentration would result in an increased rate of LWIR emission by the water, with a compensating increase in the rate of absorption of upwelling water LWIR band radiation from lower altitudes. At the same time, the increased water concentration would lead to faster ozone destruction rates and faster rates of energy

loss by OH chemiluminescence emission. The faster ozone destruction rates would lead to lower ozone concentrations and a reduction in the heating rate associated with O₃ sunlight absorption. The net result would be a reduction in temperature, of as-of-yet unknown magnitude. Any temperature decrease would lead to an increase in the sizes and lifetimes of the HLLV contrails.

B. HLLV Orbit Circularization and Deorbit Maneuvers

With the main HLLV second-stage burn confined to altitudes below 120 km, the effects on ionization in the F-layer are, as we have shown, fairly small. However, relatively small but significant amounts of H₂O and H₂ are deposited directly into the F-layer during the orbit circularization and deorbit maneuvers. The rates of exhaust emission per linear kilometer during those maneuvers are expected to be about three times the emission rate of the Centaur engine during the HEAO-C launch. Since the burn would occur at a high altitude (477 km), the efficiency for ion removal would be similarly high.

We ran a computation to represent an HLLV orbit circularization burn occurring at noon over the Philippine Islands. The assumed exhaust deposition rate was 4.9×10^{26} H₂O molecules and 1.6×10^{26} H₂ molecules per kilometer, extending over a linear distance of 1400 km. (These parameters were furnished by H. P. Davis, NASA JSC, based on expected characteristics of the HLLV orbital-maneuvering system.) After injection, the gases were assumed to fall rapidly to 270-km, while spreading crosswise to the trajectory plane over a perpendicular distance of 400 km (full width).

According to the computation, a small but definite ionospheric hole is produced, illustrated in Figs. 14a, b, and c. These figures represent a cross section perpendicular to the vehicle trajectory and lying in the geomagnetic meridian plane. The time is 2.4 hours after launch, the time of maximum ion depletion. The electron density has been reduced to one-third of its normal value over a geographic area approximately 1000 by 2000 km. The depletion lasts about five hours. The ionospheric hole would be larger and longer lasting if the launch occurred at night.

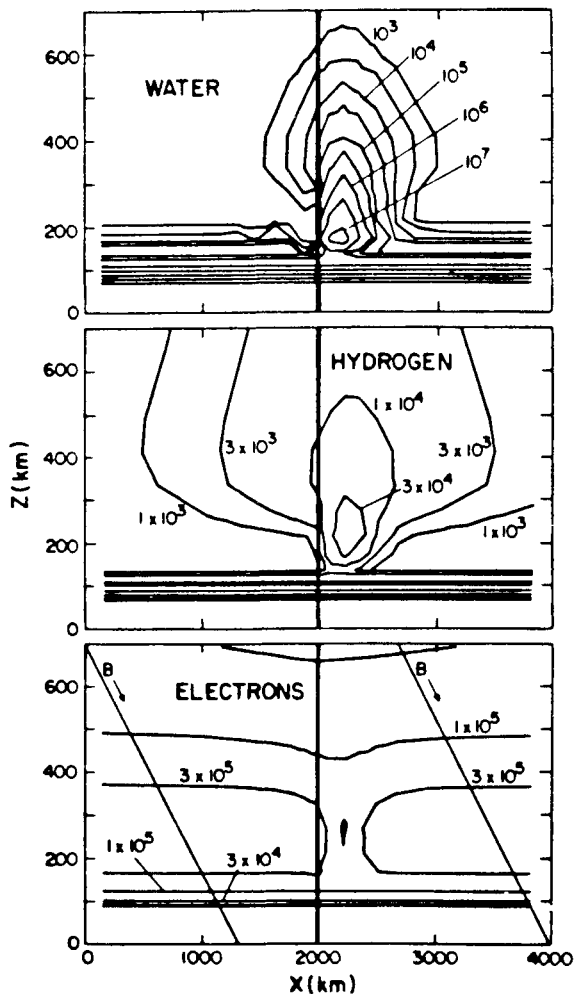


Fig. 14.

Computed concentration contours for H_2O , H_2 , and electrons (number per cubic centimeter) 2.4 hours after a hypothetical HLLV orbit circularization maneuver over the Phillipine Islands. The cross-sectional view is perpendicular to the orbital plane and parallel to the magnetic meridian plane looking back along trajectory. The original exhaust deposition was in the central plane $x = 2000$ km, and extends 1400-km lengthwise in that plane.

VI. THE COMPUTER MODEL

The computer code uses a two-dimensional array of Eulerian mesh cells in Cartesian coordinates, x horizontal (in the geomagnetic meridian plane), and z (the vertical). The range of z normally extends from 50 to 1050 km, using 15 logarithmically spaced mesh layers. The range of x is specified for each problem, usually 500 to 2000 km on either side of the rocket trajectory plane. There are 21 discrete mesh columns in x , for a total of $21 \times 15 = 315$ cells.

Conditions are assumed to be uniform in the third Cartesian direction (y). For this reason, the code is best suited to problems where the launch plane is perpendicular to the magnetic meridian (x, z) plane.

The model includes the following physical and chemical processes.

A. Chemistry

The code integrates the chemical/photochemical kinetic equations for 30 individual chemical species in each of the 315 cells. The more important reactions in the reaction set are listed in Appendix A. The chemical and photochemical rate coefficients in each cell are periodically recomputed as the temperatures and solar zenith angles change.

B. Solar radiation, scattered UV, cosmic rays, and precipitating electrons

The nominal spectral intensity of sunlight, for quiet solar conditions, in each of 81 wavelength bins, is stored within the code. Attenuation of the solar radiation in each wavelength bin at each of the 15 altitudes, due to absorption by O , O_2 , N_2 , CO_2 , and O_3 , is computed from the computed concentrations of those species and the computed solar zenith angles. The rate coefficients for photodissociation, photoionization, and photoexcitation reactions are computed from the computed spectral intensities folded with the tabulated wavelength-dependent cross sections.

Other ionization source terms are included in the model to simulate the effects of cosmic rays, precipitating Van Allen electrons, and scattered He 304-Å, Lyman α , and Lyman β radiation in the night sector.

The basic input table of solar spectral intensities is a composite of data from Ackerman,²² and Heroux and Hinteregger,²³ and represents a condition of low solar activity. Recent EUV data by Torr et al²⁴ indicate a significant increase in intensity after the onset of solar cycle 21 for wavelengths shorter than 1050 Å. The computed photoionization frequencies show a corresponding increase, almost in direct proportion to the measured 10.7-cm microwave flux. On the basis of these data, we have elected to scale all photoionization coefficients computed with the

observations.¹¹⁻¹⁶ The composite wind model is described in Appendix B. The neutral winds affect not only the drift and dispersal of contaminants in the ionosphere, such as rocket exhausts, but, through $v \times B$ forces, they exert an important influence on the vertical distribution of ionization and its normal temporal variations.

F. One-Dimensional Computations of the Normal Ionosphere

The two-dimensional code can be operated in a one-dimensional mode for computing the structure and diurnal variations of the normal ionosphere. The one-dimensional computations are used to furnish starting conditions for the two-dimensional rocket-exhaust-injection problems. These setup computations are normally run for 24 hours or more to remove transients associated with changes in the input latitude, magnetic dip angle, solar activity or season, or to compute the normal 24-hour variation of TEC.

Results of a one-dimensional computation for the 24-hour period prior to the Atlas-Centaur launch were shown in Figs. 8 and 10. Figure 10 shows the computed concentration profiles for 0130 EDT September 20 at Cape Canaveral. Figure 8 includes the computed vertical electron column density (TEC) for the 24-hour period prior to the Atlas Centaur launch.

VII. CONCLUSIONS

We have reviewed the experimental data collected on the 1979 HEAO-C launch, and compared the data with model computations. An ionospheric hole was formed with north-south dimensions of 600 to 800 km, and the hole persisted until dawn. The chemical reactions also led to enhanced 630-nm, airglow emission, which was weak but easily measurable. The size and duration of the ion depletion were in agreement with our prelaunch computations, but the airglow was brighter than expected. Post-launch improvements in the computer model have led to improved agreement.

We have also reviewed our earlier computer model results for the 1973 Skylab launch and compared those results with data of Mendillo et al. The neutral winds are a key ingredient for

explaining the apparent 4-hour duration of the Skylab F-layer hole.

With respect to predictions of ionospheric effects of SPS construction activities, we ran a model simulation of an HLLV second-stage rocket burn, and an HLLV orbit circularization burn. The principal environmentally significant effects that show up in the HLLV computations are

- a. large-scale ionospheric plasma depletions,
- b. production of massive quantities of atomic hydrogen in the thermosphere, and
- c. possible formation of persistent ice clouds near the mesopause.

The F-layer plasma depletion resulting from the main HLLV second-stage burn is less pronounced than the depletion observed after either the Skylab or HEAO-C launches. This is because the burn is confined to altitudes below 124 km. The computed electron density reduction at the F2 peak amounts to about thirty percent at night (12 hours after launch) and ten percent the following day.

The F-layer depletion resulting from the orbit circularization maneuver at LEO apogee is more severe, but relatively short-lived. The F2 peak electron density is reduced to one third of its normal value over a region approximately 1000 by 2000 km for a period of about four hours. The hole would be longer-lasting if the orbital maneuver occurred at night.

The computed rate of production of hydrogen atoms reaching the upper thermosphere (above 300-km altitude) amounts to 1.3×10^{31} per HLLV launch for the first 30-hour period. This might be sufficient to double thermospheric H-atom concentrations after six launches.

An HLLV launch would produce a large contrail in the mesosphere at about 85-km altitude, 10- to 20-km wide, and extending several hundred kilometers downrange. The contrail would persist for several hours. Repeated HLLV launches could lead to cumulative effects, which need to be investigated.

APPENDIX A
 CHEMICAL REACTIONS IN THE
 TWO-DIMENSIONAL IONOSPHERIC MODEL

Table A-I is a computer listing of the most important chemical reactions and rate parameters used in the two-dimensional code. They are a computer-selected subset of the 285 reactions actually implemented in the code. The chemical reaction rate coefficients (excluding photochemical rates) are expressed in the form

$$k = A(T/300)^B \exp(-C/T)$$

The parameters A, B, and C are tabulated for each reaction. For reactions involving only neutral molecules, the neutral temperature is used. If the reactants include electrons, the electron temperature is used. If the reactants include ions but not electrons, the ion temperature is used.

Bibliographic references for the rate data are indicated in the last column. "Reverse" means

that we have computed the rate coefficient using the computed thermodynamic equilibrium constant combined with the measured rate of the reverse reaction.

The set of 30 species is probably minimal for purposes of modeling of the E and F layers (with rocket exhaust products added). It is not sufficient for accurate modeling of the D layer, although we may compute fairly reliable D-layer electron and ion densities, nevertheless.

The photo-rate coefficients are computed as outlined in Sect. VI-B. They depend strongly on the altitude and on the time of day. A typical set of computed photo-rate coefficient vertical profiles is shown in Figs. 15a and b. They are for 12 noon local time at 28° north latitude on September 19--the day preceding the HEAO-C launch.

TABLE A-I
 THE DOMINANT CHEMICAL REACTIONS

Reactants	Products	A	B	C	References
OH CO	CO2 H	1.35E-13	0.00	0.	DEMORE (NASA), 1979
N CO2	NO CO	3.20E-13	0.00	1711.	KONDRATIEV (NBS), 1972
O3 CO	CO2 O2	4.00E-25	0.00	0.	HAMPSON (NBS), 1978
N OH	NO H	5.30E-11	0.00	0.	HAMPSON (NBS), 1978
O OH	O2 H	4.00E-11	0.00	0.	DEMORE (NASA), 1979
H O2(DL)	O OH	2.50E-14	0.00	0.	HAMPSON (NBS), 1978
H O3	OH O2	1.40E-10	0.00	470.	DEMORE (NASA), 1979
O(1D) H2	OH H	9.90E-11	0.00	0.	DEMORE (NASA), 1979
H2 O	H OH	9.00E-12	1.00	4480.	HAMPSON (NBS), 1978
O(1D) H2O	OH OH	2.30E-10	0.00	0.	DEMORE (NASA), 1979
OH OH	H2O O	1.00E-11	0.00	500.	DEMORE (NASA), 1979
OH H2	H2O H	1.20E-11	0.00	2200.	DEMORE (NASA), 1979
N O2(DL)	NO O	2.00E-14	0.00	600.	HAMPSON (NBS), 1978
O2 N(2D)	NO O	1.50E-12	.50	0.	BORTNER (DNA), 1978
O2 N(2D)	NO O(1D)	6.00E-12	.50	0.	BORTNER (DNA), 1978
N O2	NO O	4.40E-12	0.00	3220.	DEMORE (NASA), 1979
N NO	N2 O	3.40E-11	0.00	0.	DEMORE (NASA), 1979
O O3	O2 O2	1.50E-11	0.00	2218.	DEMORE (NASA), 1979
CO2 H	OH CO	4.95E-11	-.30	12321.	REVERSE
O OH	H O2(DL)	1.53E-15	0.00	3187.	REVERSE
O2 H	O OH	6.47E-10	0.00	8407.	REVERSE
H OH	H2 O	4.14E-12	1.00	3478.	REVERSE
H2O O	OH OH	4.54E-11	.40	8960.	REVERSE
O O N2	O2 N2	4.80E-33	0.00	0.	HAMPSON (NBS), 1978
O O O	O2 O(1S)	1.40E-30	0.00	650.	BORTNER (DNA), 1978
CO O M	CO2 M	6.50E-33	0.00	2180.	HAMPSON (NBS), 1978
O H M	OH M	2.00E-32	0.00	0.	HAMPSON (NBS), 1978
H H M	H2 M	8.30E-33	0.00	0.	HAMPSON (NBS), 1978
H OH M	H2O M	6.78E-31	-2.00	0.	HAMPSON (NBS), 1978
O O2 M	O3 M	1.13E-34	0.00	-510.	DEMORE (NASA), 1979
O O2 O2	O3 O2(DL)	3.02E-38	0.00	951.	REVERSE
O3 O2(SG)	O O2 O2	2.50E-11	0.00	0.	BORTNER (DNA), 1978
O3 O2(DL)	O O2 O2	6.60E-13	0.00	1560.	HAMPSON (NBS), 1978
O3 M	O O2 M	2.33E-09	0.00	11693.	REVERSE
O N	NO	1.90E-17	-.40	0.	BORTNER (DNA), 1978
N(2D)	N + HV	1.60E-05	0.00	0.	BORTNER (DNA), 1978
O(1D)	O + HV	6.80E-03	0.00	0.	BORTNER (DNA), 1978

TABLE A-I (continued)

Reactants	Products	A	B	C	References
O(1S)	O(1D) + HV	1.30E+00	0.00	0.	ALLEN, ASTRO. QUANT.
O2(SG)	O2 + HV	8.30E-02	0.00	0.	BORTNER(DNA), 1978
O2(SG)	O2(DL) + HV	2.50E-03	0.00	0.	NOXON, CAN. J. PHYS., 1961
O2(D)+	O+ + HV	1.00E-04	0.00	0.	ALLEN, ASTRO. QUANT.
E N(2D)	E N	4.32E-09	-1.10	3551.	BORTNER(DNA), 1978
O(1D) N2	O N2	2.00E-11	0.00	-107.	DEMORE (NASA), 1979
N(2D) N2	N N2	6.00E-15	0.00	0.	BORTNER(DNA), 1978
O(1S) O	O(1D) O	7.50E-12	0.00	0.	BORTNER(DNA), 1978
O(1D) O2	O O2(SG)	2.90E-11	0.00	-67.	DEMORE (NASA), 1979
O2(DL) O2	O2 O2	2.20E-18	.80	0.	BORTNER(DNA), 1978
O2 E	O2(DL) E	1.00E-11	0.00	11594.	REVERSE
O O2(SG)	O(1D) O2	3.39E-11	-1.10	4201.	REVERSE
O N(2D)	E NO+	7.60E-13	0.00	4162.	REVERSE
E H+	H	3.50E-12	-1.70	0.	BORTNER(DNA), 1978
E NO+	NO	4.00E-12	-1.70	0.	BORTNER(DNA), 1978
E NO+ M	NO M	6.00E-27	-2.50	0.	BORTNER(DNA), 1978
E OH+	O H	1.73E-07	0.00	0.	SUTHERLAND, 1975
E OH+	O(1D) H	2.20E-08	0.00	0.	SUTHERLAND, 1975
E OH+	O(1S) H	4.40E-09	0.00	0.	SUTHERLAND, 1975
E H2O+	O H2	2.00E-08	0.00	0.	SUTHERLAND, 1975
E H2O+	H2 O(1D)	1.00E-08	0.00	0.	SUTHERLAND, 1975
E H2O+	OH H	1.70E-07	0.00	0.	SUTHERLAND, 1975
E H3O+	H H2O	1.30E-06	-1.70	0.	BORTNER(DNA), 1978
E NO+	O N(2D)	4.00E-07	-1.00	0.	BORTNER(DNA), 1978
E N2+	N N(2D)	1.80E-07	-1.40	0.	BORTNER(DNA), 1978
E O2+	O O(1D)	1.89E-07	-1.60	0.	BORTNER(DNA), 1978
E O2+	O(1S) O	2.10E-08	-1.60	0.	BORTNER(DNA), 1978
N+ H	H+ N	3.60E-12	0.00	0.	CONSTANTINIDES, 1979
H+ NO	NO+ H	1.90E-09	0.00	0.	BORTNER(DNA), 1978
OH+ NO	NO+ OH	3.00E-10	0.00	0.	J. ZINN ESTIMATE
N2+ H	H+ N2	3.00E-10	0.00	0.	J. ZINN ESTIMATE
N2+ OH	OH+ N2	3.00E-10	0.00	0.	J. ZINN ESTIMATE
O+ H	H+ O	6.80E-10	0.00	0.	BORTNER(DNA), 1978
H+ O2	O2+ H	5.00E-10	0.00	0.	W. MAIER ESTIMATE
O+ OH	OH+ O	3.00E-10	0.00	0.	J. ZINN ESTIMATE
OH+ O2	O2+ OH	2.00E-10	0.00	0.	BORTNER(DNA), 1978
N+ H2O	H2O+ N	2.60E-09	0.00	0.	BORTNER(DNA), 1978
H2O+ NO	NO+ H2O	3.00E-10	0.00	0.	J. ZINN ESTIMATE
N2+ H2O	H2O+ N2	6.10E-10	0.00	0.	TIERNAN, 1969
O+ H2O	H2O+ O	2.30E-09	0.00	0.	BORTNER(DNA), 1978
H2O+ O2	O2+ H2O	2.00E-10	0.00	0.	BORTNER(DNA), 1978
H+ H2O	H2O+ H	3.00E-10	0.00	0.	J. ZINN ESTIMATE
HE+ N2	N2+ HE	7.00E-10	0.00	0.	BANKS AND KOCKARTS
N+ O	O+ N	2.20E-12	0.00	0.	CONSTANTINIDES, 1979
O+ N(2D)	N+ O	1.30E-10	0.00	0.	CONSTANTINIDES, 1979
N+ O2	O2+ N	2.80E-10	0.00	0.	BORTNER(DNA), 1978
O2+ NO	NO+ O2	4.50E-10	0.00	0.	BORTNER(DNA), 1978
N2+ O	O+ N2	1.00E-11	-1.20	0.	BORTNER(DNA), 1978
N+ NO	NO+ N	8.00E-10	0.00	0.	BORTNER(DNA), 1978
O(2D)+ N2	N2+ O	1.00E-09	0.00	0.	BANKS AND KOCKARTS
N2+ O2	O2+ N2	5.00E-10	-1.80	0.	BORTNER(DNA), 1978
N2+ NO	NO+ N2	3.70E-10	0.00	0.	BORTNER(DNA), 1978
O+ O2	O2+ O	2.00E-11	-1.40	0.	BORTNER(DNA), 1978
H+ O	O+ H	7.73E-10	-1.10	215.	REVERSE
O+ CO2	O2+ CO	1.10E-09	0.00	0.	BORTNER(DNA), 1978
O+ OH	O2+ H	1.00E-09	0.00	0.	ESTIMATE
O+ H2	OH+ H	2.00E-09	0.00	0.	BORTNER(DNA), 1978
OH+ H2	H2O+ H	1.50E-09	0.00	0.	FEHSENFELD, 1967
OH+ H2O	H3O+ O(1D)	1.50E-09	0.00	0.	GUPTA, 1967
H2O+ H2	H3O+ H	1.40E-09	0.00	0.	FEHSENFELD, 1967
H2O+ H2O	H3O+ OH	1.80E-09	0.00	0.	BORTNER(DNA), 1978
HE+ N2	N+ N HE	7.00E-10	0.00	0.	BANKS AND KOCKARTS
HE+ O2	O+ O HE	1.50E-09	0.00	0.	BANKS AND KOCKARTS
N+ O2	NO+ O	2.80E-10	0.00	0.	BORTNER(DNA), 1978
O2+ N	NO+ O2	1.20E-10	0.00	0.	BORTNER(DNA), 1978
N+ O3	NO+ O2	5.00E-10	0.00	0.	W. MAIER ESTIMATE
O+ N2	NO+ N	1.20E-12	-1.00	0.	BORTNER(DNA), 1978
N2+ O	NO+ N	1.30E-10	-1.50	0.	BORTNER(DNA), 1978
O2+ N2	NO+ NO	1.00E-16	0.00	0.	BORTNER(DNA), 1978
O2+ CO	O+ CO2	2.91E-11	.10	14130.	REVERSE
O+ OH	H+ O2	2.70E-11	.10	0.	REVERSE
CO2 + HV	CO O				BORTNER(DNA), 1978
H2O + HV	H OH				BORTNER(DNA), 1978
NO + HV	N O				PARK, 1974
N2 + HV	N N				HUFFMAN, 1969
N2 + HV	N N(2D)				HUFFMAN, 1969
O2 + HV	O O				BORTNER(DNA), 1978
O2 + HV	O O(1D)				KOCKARTS, 1976
O3 + HV	O2(DL) O				ACKERMAN, 1971
O3 + HV	O2(DL) O(1D)				ACKERMAN, 1971
O + HV	O(1S)				ALLEN, ASTRO. QUANT.
O2 + HV	O2(DL)				BORTNER(DNA), 1978
O2 + HV	O2(SG)				BORTNER(DNA), 1978
H + HV	H+ E				W. HUEBNER, PR. COMM.
HE + HV	HE+ E				TORR ET AL., 1979
N + HV	N+ E				W. HUEBNER, PR. COMM.
N(2D) + HV	N+ E				W. HUEBNER, PR. COMM.
N2 + HV	N2+ E				W. HUEBNER, PR. COMM.

TABLE A-I (continued)

Reactants		Products		A	B	C	References
N ₂	+ hv	N+	E				W. HUEBNER, PR. COMM.
O	+ hv	O+	E				W. HUEBNER, PR. COMM.
O	+ hv	O(2D)+	E				TORR ET AL., 1979
O ₂	+ hv	O ₂ +	E				W. HUEBNER, PR. COMM.

APPENDIX B

THE TRANSPORT EQUATIONS

1. GLOSSARY OF TERMS

Coordinates and velocities:

- x = horizontal coordinate in magnetic meridian plane (northward)
- y = coordinate perpendicular to meridian plane (westward)
- z = vertical coordinate
- u = x velocity
- v = y velocity
- w = z velocity

Species subscripts:

- e = electrons
- + = positive ions
- n = neutrals
- i = ith individual species
- n(n_e, n₊, n_n, n_i) = number densities
- p(p_e, p₊, p_i) = partial pressures
- T(T_e, T₊, T_n) = temperatures
- v(v_e, v_i) = collision frequencies
- Ω(Ω_e, Ω_i) = gyrofrequencies
- m(m_e, m_i, \bar{m} , \bar{m}_+) = species mass
- H(H_i, \bar{H} , \bar{H}_+) = scale heights
- D(D_{in}, D_{ai}, D_{eddy}) = diffusion coefficients
- t = time
- λ = latitude
- I = magnetic dip angle
- δ = magnetic declination
- B_x, B_z = magnetic field components
- E_x, E_y, E_z = electric field components
- k = Boltzmann's constant
- g = gravitational constant
- e = electron charge
- c = speed of light

2. NEUTRAL WIND VELOCITIES

The neutral temperatures are assumed to vary with z and t in a prescribed manner, derived from fits to model atmosphere data. If overall hydrostatic equilibrium is assumed, it can be shown

that the macroscopic average vertical wind velocity must be given by the differential equation

$$\frac{\partial \bar{w}_n}{\partial z} - \bar{w}_n \frac{\partial \ln \bar{H}}{\partial z} = \frac{\partial \ln \bar{H}}{\partial t}, \quad (B-1)$$

where $\bar{H} = (kT_n/\bar{m}g)$ and

$$\bar{m} = \frac{\sum_i n_i m_i}{\sum_i n_i}.$$

The solution of Eq. (B-1) is

$$\bar{w}_n = \bar{H} \int_{z_0}^z \frac{1}{\bar{H}^2} \frac{\partial \bar{H}}{\partial t} dz, \quad (B-2)$$

which can be evaluated by quadrature.

The horizontal neutral wind components \bar{v}_N (toward the north) and \bar{v}_W (toward the west) are represented as linear superpositions of seasonal average, diurnal (S_{11} and $S_{1,-2}$ modes) and semidiurnal terms. The separate terms are generated from fits to the data of R. M. Harper²⁷ and of P. Amayenc²⁸ and computations of Roble et al.¹⁵ and of Forbes and Garrett.^{12,13,14} We are grateful for the advice of R. M. Harper, J. M. Forbes, and H. B. Garrett.

We represent the meridional wind component as

$$\bar{v}_N = A_{0N} - A_{11N} \cos[2\pi(\tau - \Delta_{11N})/24] - A_{12N} \cos[2\pi(\tau - \Delta_{12N})/24] - A_{2N} \cos[2\pi(\tau - \Delta_{2N})/12],$$

where τ is the time of day in hours and the subscripts 11N, 12N, and 2N refer respectively to the diurnal S_{11} mode, diurnal $S_{1,-2}$ mode, and the semidiurnal mode. A_{0N} is the seasonal average northward velocity. The A's and Δ's are generated as fitted functions of altitude, latitude, time of year, and solar activity level, or a subset of these variables.

The seasonal average term A_{0N} is generated with a computer subroutine that was kindly furnished by J. M. Forbes. It is based on fits to results of computations by Roble, Dickinson, and Ridley.¹⁵

Values of the parameters A_{11N} , A_{12N} , A_{2N} , Δ_{11N} , Δ_{12N} , and Δ_{2N} were determined as functions of altitude by R. M. Harper^{16,27} from incoherent scatter measurements at Arecibo for solar minimum non-winter conditions. We have fitted Harper's data with approximate analytic functions of altitude. Of the two diurnal modes S_{11} and $S_{1,-2}$, the former is dominant at low latitudes, while the latter dominates at high latitudes. We deduced the relative strengths of the two modes as functions of latitude from the computations of Forbes and Garrett.¹² We use Forbes' and Garrett's results to scale Harper's Arecibo values of A_{11N} and A_{12N} to non-Arecibo latitudes. The scaled amplitudes lead to reasonable agreement with the computations of Forbes and Garrett for solar minimum conditions at 45° latitude. For solar maximum conditions, A_{11N} increases at low latitudes (R. M. Harper, private communication²⁷). The quantities A_{2N} , Δ_{11N} , Δ_{12N} , and Δ_{2N} are all assumed, for lack of detailed information, to be independent of latitude, season, and solar activity.

For the zonal wind system, \bar{v}_w , we again use a linear superposition of seasonal average, diurnal, and semidiurnal terms; i.e.,

$$\bar{v}_w = A_{0W} + A_{1W} \cos[2\pi(\tau - \Delta_{1W})/24] + A_{2W} \cos[2\pi(\tau - \Delta_{2W})/12] ,$$

where A_{0W} is the seasonal average velocity, and the subscripts 1W and 2W refer to diurnal and semidiurnal modes. A_{0W} is computed with a subroutine supplied by J. M. Forbes. The diurnal amplitude A_{1W} is assumed to be the same as A_{12N} , the amplitude of the meridional component of the $S_{1,-2}$ mode. The phase shift Δ_{1W} is set equal to -4 hours. For the semidiurnal mode, we assume $A_{2W} = 25$ m/s and $\Delta_{12} = 6$ hours, independent of altitude, latitude, and season.

The velocity components \bar{v}_N and \bar{v}_W , which are in geographic coordinates, must be transformed to geomagnetic coordinates (x,y,z) via

$$\bar{u}_n = \bar{v}_N \cos \delta + \bar{v}_W \sin \delta , \quad (B-3)$$

and

$$\bar{v}_n = -\bar{v}_N \sin \delta + \bar{v}_W \cos \delta , \quad (B-4)$$

where \bar{u}_n and \bar{v}_n are the macroscopic average neutral wind velocities in the magnetic coordinate system.

3. NEUTRAL SPECIES TRANSPORT

The quasi-steady velocity components for the i^{th} neutral species above the turbopause are

$$u_i = \bar{u}_n - D_{in} \frac{\partial \ln p_i}{\partial x} , \quad (B-5)$$

$$v_i = \bar{v}_n - D_{in} \frac{\partial \ln p_i}{\partial y} , \quad (B-6)$$

and

$$w_i = \bar{w}_n - D_{in} \left[\frac{\partial \ln p_i}{\partial z} + \frac{1}{H_i} \right] , \quad (B-7)$$

where $p_i = n_i k T_n$, and $H_i = k T_n / m_i g$, and D_{in} is the molecular diffusion coefficient of species i .

Below the turbopause (~100-km altitude) the eddy diffusion coefficient, D_{eddy} , is larger than the molecular diffusion coefficients. In that altitude range, the equations must be modified by replacing H_i with \bar{H} and replacing D_{in} by D_{eddy} . Although we have included the term $\partial \ln p_i / \partial y$ in Eq. (B-6), we assume, for the present two-dimensional model, that $\partial / \partial y = 0$.

The rate of change of the i^{th} species concentration is computed as

$$\frac{\partial n_i}{\partial t} = -\nabla \cdot (n_i \vec{v}_i) + P_i - L_i , \quad (B-8)$$

where P_i and L_i are the chemical production and loss terms.

4. ION TRANSPORT EQUATIONS

We assume that the equations of motion for ions and electrons (in Gaussian emu) are approximated adequately by

$$-\frac{1}{n_i m_i} \nabla p_i + \frac{e}{m_i} \left\{ \vec{E} + \frac{\vec{v}_i \times \vec{B}}{c} \right\} - \hat{z}g - v_i (\vec{v}_i - \vec{v}_n) = 0 \quad (\text{B-9})$$

and

$$-\frac{1}{n_e m_e} \nabla p_e - \frac{e}{m_e} \left\{ \vec{E} + \frac{\vec{v}_e \times \vec{B}}{c} \right\} - \hat{z}g - v_e (\vec{v}_e - \vec{v}_n) = 0 \quad (\text{B-10})$$

respectively. We have ignored the inertial terms $d\vec{v}_i/dt$ and $d\vec{v}_e/dt$, and we have ignored electron-ion collisions. It will be helpful to transform to coordinates moving with the neutral velocity \vec{v}_n . The transformed ion and electron velocities are $\tilde{v}_i = \vec{v}_i - \vec{v}_n$ and $\tilde{v}_e = \vec{v}_e - \vec{v}_n$ with components $\tilde{u}_i, \tilde{v}_i, \tilde{w}_i$, and $\tilde{u}_e, \tilde{v}_e, \tilde{w}_e$. The transformed E field is $\tilde{E} = \vec{E} + \vec{v}_n \times \vec{B}/c$, with components \tilde{E}_x, \tilde{E}_y , and \tilde{E}_z . We will also introduce the Larmor frequencies $\Omega_i = |eB/m_i c|$ and $\Omega_e = |eB/m_e c|$ and their components $\Omega_{ix}, \Omega_{iy}, \Omega_{iz}, \Omega_{ex}, \Omega_{ey}$, and Ω_{ez} where $\Omega_{ix} = |e|B_x/m_i c$, etc.

We will confine the discussion to a two-dimensional system in a magnetic meridian (x,z) plane, such that $B_y = 0$ and $\partial/\partial y = 0$ and the magnetic field lines are assumed to be straight and parallel. Then, in matrix form and in terms of the transformed variables, Eqs. (B-9) and (B-10) become

$$\begin{bmatrix} v_i & -\Omega_{iz} & 0 \\ \Omega_{iz} & v_i & -\Omega_{ix} \\ 0 & \Omega_{ix} & v_i \end{bmatrix} \begin{bmatrix} \tilde{u}_i \\ \tilde{v}_i \\ \tilde{w}_i \end{bmatrix}$$

$$= \begin{bmatrix} e\tilde{E}_x/m_i - \partial p_i/\partial x/n_i m_i \\ e\tilde{E}_y/m_i \\ e\tilde{E}_z/m_i - \partial p_i/\partial z/n_i m_i - g \end{bmatrix} \quad (\text{B-11})$$

and

$$\begin{bmatrix} v_e & \Omega_{ez} & 0 \\ -\Omega_{ez} & v_e & \Omega_{ex} \\ 0 & -\Omega_{ex} & v_e \end{bmatrix} \begin{bmatrix} \tilde{u}_e \\ \tilde{v}_e \\ \tilde{w}_e \end{bmatrix} = \begin{bmatrix} -e\tilde{E}_x/m_e - \partial p_e/\partial x/n_e m_e \\ -e\tilde{E}_y/m_e \\ -e\tilde{E}_z/m_e - \partial p_e/\partial z/n_e m_e - g \end{bmatrix} \quad (\text{B-12})$$

If the quantities on the right-hand side are regarded as known, these equations can be inverted to give $\tilde{u}_i, \tilde{v}_i, \tilde{w}_i, \tilde{u}_e, \tilde{v}_e, \tilde{w}_e$. For present purposes, we will disregard \tilde{v}_i and \tilde{v}_e . The inverted equations are

$$\begin{aligned} \tilde{u}_i &= a_i (e\tilde{E}_x - \frac{1}{n_i} \frac{\partial p_i}{\partial x}) \\ &- b_i (e\tilde{E}_z - \frac{1}{n_i} \frac{\partial p_i}{\partial z} - m_i g) - c_i (e\tilde{E}_y), \end{aligned} \quad (\text{B-13a})$$

$$\begin{aligned} \tilde{w}_i &= -b_i (e\tilde{E}_x - \frac{1}{n_i} \frac{\partial p_i}{\partial x}) \\ &+ f_i (e\tilde{E}_z - \frac{1}{n_i} \frac{\partial p_i}{\partial z} - m_i g) - d_i (e\tilde{E}_y), \end{aligned} \quad (\text{B-13b})$$

$$\begin{aligned} \tilde{u}_e &= a_e (-e\tilde{E}_x - \frac{1}{n_e} \frac{\partial p_e}{\partial x}) \\ &- b_e (-e\tilde{E}_z - \frac{1}{n_e} \frac{\partial p_e}{\partial z} - m_e g) - c_e (e\tilde{E}_y), \end{aligned} \quad (\text{B-14a})$$

$$\tilde{w}_e = -b_e (-e\tilde{E}_x - \frac{1}{n_e} \frac{\partial p_e}{\partial x})$$

$$+ f_e(-e\tilde{E}_z - \frac{1}{n_e} \frac{\partial p_e}{\partial z} - m_e g) - d_e(e\tilde{E}_y), \quad (\text{B-14b})$$

where the coefficients $a_i \dots f_i$, $a_e \dots f_e$ are (for a_i use v_i , Ω_i , m_i , and for a_e use v_e , Ω_e , m_e)

$$a = \frac{(v^2 + \Omega_x^2)}{mv(v^2 + \Omega^2)} \quad (\text{B-15a})$$

$$b = \frac{-\Omega_x \Omega_z}{mv(v^2 + \Omega^2)} \quad (\text{B-15b})$$

$$c = \frac{-v\Omega_z}{mv(v^2 + \Omega^2)} \quad (\text{B-15c})$$

$$d = \frac{v\Omega_x}{mv(v^2 + \Omega^2)} \quad (\text{B-15d})$$

$$f = \frac{(v^2 + \Omega_z^2)}{mv(v^2 + \Omega^2)} \quad (\text{B-15e})$$

Now it is necessary to supply values of \tilde{E}_x , \tilde{E}_y , and \tilde{E}_z . We invoke the familiar quasi-charge-neutrality assumptions

$$n_e = \sum_i n_i. \quad (\text{B-16})$$

and

$$\nabla \cdot \vec{j} = 0, \quad (\text{B-17})$$

where

$$\vec{j} = \frac{e}{c} (\sum_i n_i \vec{v}_i - n_e \vec{v}_e). \quad (\text{B-18})$$

Our first problem will be to generate vertical profiles for the normal ionosphere. With some justification, we can treat this as a one-dimensional problem with $\partial/\partial x = \partial/\partial y = 0$. In that case, Eq. (B-17) becomes

$$\frac{\partial j_z}{\partial z} = 0, \text{ or } j_z \text{ constant.} \quad (\text{B-19a})$$

Since there can be no vertical current at the bottom boundary, the constant of integration is zero and

$$j_z = 0. \quad (\text{B-19b})$$

This is equivalent to the statement that

$$\sum_i n_i \tilde{w}_i - n_e \tilde{w}_e = 0. \quad (\text{B-20})$$

If we combine this equation with Eqs. (B-13), (B-14), and (B-15), we can obtain self-consistent solutions for \tilde{u}_i , \tilde{w}_i , \tilde{u}_e , \tilde{w}_e , and \tilde{E}_z , if \tilde{E}_x , \tilde{E}_y and the pressure gradients are assumed to be known. The equation for $e\tilde{E}_z$ is

$$\begin{aligned} e\tilde{E}_z = & [e\tilde{E}_x (n_e b_e + \sum_i n_i b_i) \\ & - f_e (\frac{\partial p_e}{\partial z} + n_e m_e g) + \sum_i f_i (\frac{\partial p_i}{\partial z} + n_i m_i g) \\ & - e\tilde{E}_y (n_e d_e - \sum_i n_i d_i)] / (n_e f_e + \sum_i n_i f_i) \end{aligned} \quad (\text{B-21})$$

For a truly one-dimensional ionosphere, we would expect that $E_x = E_y = 0$, so that

$$\tilde{E}_x = v_n B_z / c \quad (\text{B-22a})$$

and

$$\tilde{E}_y = \frac{1}{c} (w_n B_x - u_n B_z). \quad (\text{B-22b})$$

In that case, $e\tilde{E}_z$ can be evaluated immediately with Eq. (B-21). Then, upon substituting $e\tilde{E}_x$, $e\tilde{E}_y$, and $e\tilde{E}_z$ into Eq. (B-13b), one can evaluate the ion vertical velocities \tilde{w}_i , and $w_i = \tilde{w}_i + w_n$. The rate of change of the i^{th} species concentration is

$$\frac{\partial n_i}{\partial t} = - \frac{\partial}{\partial z} (n_i w_i) + P_i - L_i, \quad (\text{B-23})$$

where P_i and L_i are the chemical production and loss rates. Therefore, the n_i can be integrated forward in time when the w_i are known. The electron concentration $n_e = \sum n_i$ [Eq. (B-16)]. The electron and ion partial pressures are

$$p_i = n_i k T_i \quad (B-24a)$$

and

$$p_e = n_e k T_e \quad (B-24b)$$

The electron and ion temperatures are specified separately as functions of z and t , as are the neutral velocities u_n , v_n , and w_n .

Thus, for a one-dimensional ionosphere, Eqs. (B-13) through (B-24) and the coupled chemical kinetics equations constitute a closed set, which can be integrated to generate sets of concentration profiles as functions of time.

For a two-dimensional ionosphere, the equations are considerably more complicated. This is primarily because $\nabla \cdot \vec{j}$ is no longer equal to just $\partial j_z / \partial z$, and we can no longer set $E_x = E_y = 0$. However, we can make a simple and accurate approximation.

Examination of the separate terms in Eq. (B-21) reveals that at latitudes not too near the geomagnetic equator

$$eE_z \approx -\frac{1}{n_e} \frac{\partial p_e}{\partial z};$$

that is, the ambipolar term is dominant. For the same physical reasons, the ambipolar term should dominate in eE_x . That is, we may assume

$$eE_x = -\frac{1}{n_e} \frac{\partial p_e}{\partial x}, \quad (B-25)$$

and continue to assume $j_z = 0$. The new equation for $e\tilde{E}_z$ is

$$e\tilde{E}_z = \left[\frac{e}{c} v_n B_z (n_e b_e + \sum_i n_i b_i) - \sum_i n_i b_i \left(\frac{1}{n_e} \frac{\partial p_e}{\partial x} + \frac{1}{n_i} \frac{\partial p_i}{\partial x} \right) \right]$$

$$- f_e \left(\frac{\partial p_e}{\partial z} + n_e m_e g \right) + \sum_i f_i \left(\frac{\partial p_i}{\partial z} + n_i m_i g \right) - e\tilde{E}_y (n_e d_e - \sum_i n_i d_i) / (n_e f_e + \sum_i n_i f_i) \quad (B-26)$$

We assume, as before that $E_y = 0$, and \tilde{E}_y is given by Eq. (B-22b). Then Eqs. (B-13) through (B-16), (B-22b), (B-24), and (B-26) constitute a closed set for determining the ion velocities u_i and w_i . The rate of change of the i^{th} species concentration is

$$\frac{\partial n_i}{\partial t} = -\frac{\partial}{\partial x} (n_i u_i) - \frac{\partial}{\partial z} (n_i w_i) + P_i - L_i \quad (B-27)$$

The magnetic dip angle is I , assumed to be positive in the northern hemisphere; x is the magnetic northward direction, and \hat{B} is the xz plane. $B_x = B \cos I$, $B_z = -B \sin I$, $\Omega_{ex} = \Omega_e \cos I$, $\Omega_{ez} = -\Omega_e \sin I$, $\Omega_{ix} = \Omega_x \cos I$, and $\Omega_{iz} = -\Omega_i \sin I$.

There should be nothing startling in these equations. They are a straightforward extension of those given by Banks and Kockarts²⁵ (Vol. B, Chapt. 19, 20) and other authors.

5. Boundary Conditions

The concentrations of N_2 , O_2 , CO_2 , H_2O , H_2 , He , and NO are held constant in the bottom row of mesh cells. For all other species, the bottom boundary fluxes are set to zero. In this connection, it is relevant to note that the photochemical time constants of odd oxygen and odd hydrogen species at 50-km altitude are less than one hour, whereas the time constant for odd nitrogen is about 100 days.

The horizontal boundary flux conditions are recursive; that is, the fluxes at the left boundary at each altitude are set equal to the corresponding fluxes at the right-hand boundary.

In the top row of mesh cells, we assume that all species are in hydrostatic equilibrium. That is, all concentrations in the top row of cells are related directly to the concentrations in the row below according to the diffusive equilibrium relationship

$$n_{i2} = n_{i1} (T_1/T_2) \exp \left\{ - \int_{z1}^{z2} dz / H_i \right\}, \quad (B-28)$$

where subscript 2 refers to the top cell (median altitude z_2), and subscript 1 refers to the cell below (median altitude z_1). For neutrals, T_1 and T_2 are the neutral gas temperatures T_n , and H_i is the neutral scale height $kT_n/m_i g$. For ions, the temperatures are the sums of ion and electron temperatures, $T_+ + T_e$, and H_i is the ion scale height given by

$$H_i = \frac{k}{g} \left[\frac{T_+(T_e + T_+)}{m_i(T_e + T_+) - m_+T_e} \right] \quad (B-29)$$

where m_+ is the average ion mass.

6. Input Conditions

To begin a two-dimensional computation involving deposition of rocket exhaust products, we must first compute the vertical structure of the ambient ionosphere and neutral atmosphere, as appropriate for the given geographic location, time of year, solar activity condition, and time of day or night. This is done by running the code in the one-dimensional mode for a period of at least 24 hours, starting from some previously computed ionosphere, evolved over a week or more of problem time. At the appropriate time the ambient ionospheric profiles are loaded into the two-dimensional computing mesh and the rocket exhaust products are added.

In most cases of interest, the molecular collision mean-free paths at the rocket trajectory altitude are long compared to dimensions of the numerical mesh cells. In such cases the initial spreading and settling of the exhaust cloud cannot be approximated adequately by the diffusion algorithms described in Sects. B-3 and B-4 above. Therefore, to set up the problem, we start with an algorithm that represents a ballistic expansion modified by gravity and molecular collisions. The ballistic algorithm is based on the following.

The exhaust injection is assumed to be cylindrically symmetric about the trajectory direction, which is perpendicular to the (x,z) plane of the computation. The distribution of initial velocities of the exhaust molecules is described by a cylindrical Maxwellian corresponding to a specified exit temperature T_x ($T_x \sim 1000$ to 1500 K). That is

$$dN = N_0 \left(\frac{m}{2\pi kT_x} \right) e^{-m(u_0^2 + w_0^2)/2kT_x} du_0 dw_0 \quad (B-30)$$

is the number of molecules with initial velocities between u_0 and $u_0 + du_0$ and between w_0 and $w_0 + dw_0$, and N_0 is the total number of molecules. The x and z components of the equation of motion of a molecule are assumed to be

$$\frac{du}{dt} = -\nu u \quad (B-31)$$

$$\frac{dw}{dt} = -\nu w - g \quad (B-32)$$

where ν is the collision frequency. If these equations can be integrated, then for any specified position (x,z) and time t we can solve, in principle, for the initial velocity components u_0 and w_0 . Then by application of the Liouville equation, we can find the spatial density of molecules at (x,z,t) . That is

$$n(x,z,t) = N_0 \left(\frac{m}{2\pi kT_x} \right) e^{-m(u_0^2 + w_0^2)/2kT_x} \frac{du_0 dw_0}{dx dz}, \quad (B-33)$$

where u_0 , w_0 , and $(du_0 dw_0 / dx dz)$ are now known functions of x , z , and t .

The equations of motion are simplified greatly if we assume that the collision frequency ν is constant. Then they can be integrated exactly and solved for u_0 and w_0 . If, at $t = 0$, $x = 0$, and $z = z_0$, we obtain

$$u_0 = \frac{vx}{1 - e^{-\nu t}}, \quad (B-34)$$

$$w_0 = \frac{-\frac{g}{\nu}(1 - e^{-\nu t}) + \nu(z - z_0) + gt}{1 - e^{-\nu t}}, \quad (B-35)$$

and

$$\frac{du_0 dw_0}{dx dz} = \left(\frac{\nu}{1 - e^{-\nu t}} \right)^2, \quad (B-36)$$

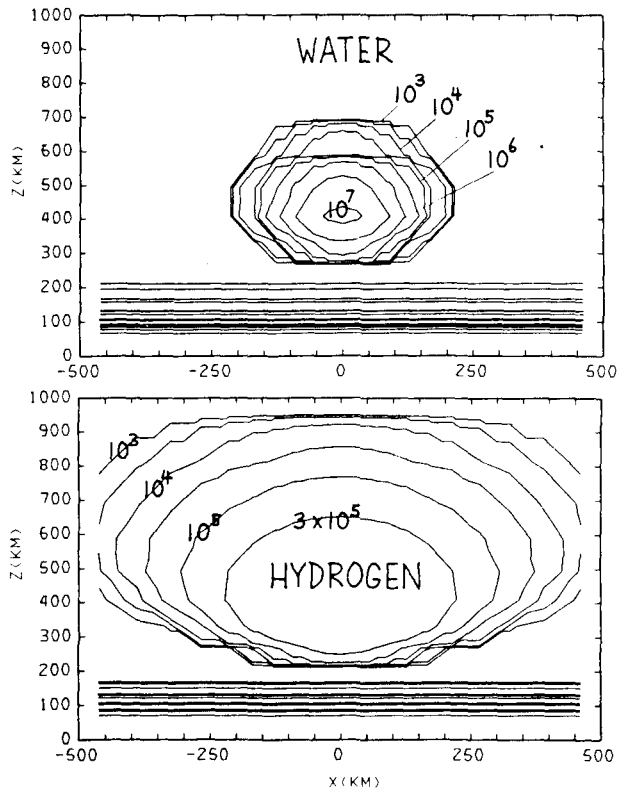


Fig. 16.

Computed contours of H_2 and H_2O concentrations from HEAO-C in a magnetic meridian plane 1500-km downrange from the launch point 100 s after passage of the rocket (11 min after launch). The contours were computed with the ballistic model with $z_0 = 460$ km and $T_x = 1400$ K.

and these expressions can be substituted in Eq. (B-33) to give $n(x,z,t)$.

Of course ν is by no means constant, being proportional to the local atmospheric number density. Nevertheless, we can obtain useful approximate results with Eqs. (B-33) to (B-36) if we use an effective average ν which depends on the particle path.

Our objective is simply to compute the (approximate) number densities of molecules at positions (x,y) at an early time t . The number of collisions experienced by a molecule by the time t when it reaches (x,z) is $\bar{\nu}t = \int \nu dt = \int ds/\lambda$, where λ is the local mean-free path and the last integral is along the molecule's trajectory in x,z . If we assume $\lambda = \lambda_0 \exp[(z-z_0)/H]$, where λ_0 is the mean-free path at z_0 and H is the scale height, and if we approximate the trajectory by a straight line, we obtain

$$\bar{\nu}(x,z,z_0,t) =$$

$$\frac{H}{\lambda_0 t} \left[\frac{x^2 + (z - z_0)^2}{(z - z_0)^2} \right]^{1/2} \left| 1 - e^{-(z-z_0)/H} \right|. \quad (B-37)$$

Using Eqs. (B-33) through (B-37), we can compute $n(x,z,t)$ if z_0 , N_0 , T_x , and the molecular mass, m , are given.

Figure 16 shows the computed distributions of H_2O and H_2 molecules for the case of HEAO-C in a plane 1500-km downrange, 100-s after passage of the rocket, as computed with the ballistic algorithm, Eqs. (B-33) to (B-37). The trajectory altitude $z_0 = 460$ km, and we have assumed $T_x = 1400$ K.

REFERENCES

1. M. Mendillo, G. S. Hawkins, and J. A. Klobuchar, "A Sudden Vanishing of the Ionospheric F Region Due to the Launch of Skylab," *J. Geophys. Res.* **80**, 2217-2228 (June 1975).
2. M. Mendillo, G. S. Hawkins, and J. A. Klobuchar, "A Large Scale Hole in the Ionosphere Caused by the Launch of Skylab," *Science* **187**, 343 (1975a).
3. J. M. Forbes and M. Mendillo, "Diffusion Aspects of Ionospheric Modification by the Release of Highly Reactive Molecules into the F-Region," *J. Atm. Terr. Phys.* **38**, 1299-1307 (1976).
4. M. Mendillo and J. M. Forbes, "Artificially Created Holes in the Ionosphere," *J. Geophys. Res.* **83**, 151-162 (1978).
5. NASA, "Satellite Power System, Concept Development and Evaluation Program," Reference System Report, US Department of Energy, DOE/ER-0023, (October 1978).
6. J. Zinn and C. D. Sutherland, "Effects of Rocket Exhaust Products in the Thermosphere and Ionosphere," Los Alamos Scientific Laboratory report LA-8233-MS (February 1980).
7. J. Zinn and C. D. Sutherland, "Effects of Rocket Exhaust Products in the Thermosphere and Ionosphere," *Space Solar Power Review* **1**, 109-132 (1980).
8. M. Mendillo, J. Baumgardner, and J. A. Klobuchar, "Opportunity to Observe a Large-Scale Hole in the Ionosphere," *EOS* **60**, 513 (July 1979).

9. Proceedings of the Symposium Workshop on the Launch of HEAO-C, Boston, November 11-13, 1979 (Sponsored by DoE Solar Power Satellite Project Office), M. Mendillo, ed. (in press). The following papers are included:
 - a. J. Baumgardner, B. Vance, M. Mendillo, and J. Klobuchar, "Multi-Station TEC Observations of the HEAO-Hole using the SIRIO Satellite"
 - b. P. Bernhardt, et al, "Multi-Station TEC Observations of the HEAO-Hole using the SIRIO Satellite"
 - c. J. Goodman, "An Overview of the NRL Radio Propagation Studies Undertaken in Conjunction with the HEAO-Hole Experiment"
 - d. J. Goodman, M. Reilly, A. Martin, E. Bird, and A. Richards, "Trans-Ionospheric Radiowave Propagation Studies Performed at Bermuda during the Late Summer of 1979"
 - e. M. Reilly, "Implications of NRL Polarimetry Data for the Dynamics of Ionospheric Electron Hole Generation of HEAO-C"
 - f. H. Soicher and F. Gorman, "TEC Observations of the HEAO-Hole using SIRIO and ATS-5"
 - g. M. Mendillo and P. Bernhardt, "Discussion of Unified TEC Morphologies - Joint Data Presentation Techniques"
 - h. J. Clynch, "Spatial Variations of the HEAO-Hole from Differential Doppler Measurements"
 - i. I. Kofsky, D. Villanuucci, E. Huppi, and R. Huppi, "Optical and Infrared Measurements from a KC-135 Aircraft of the Intensity and Extent of the Afterglows Excited by the Centaur Molecule Releases"
 - j. R. Wand and M. Mendillo, "Millstone Hill Incoherent Scatter Observations of the HEAO-C Induced Ionospheric Hole"
 - k. L. Duncan, R. Behnke, and J. Zinn, "Arecibo Radar Observations of the HEAO-C Atlas/Centaur Launch"
 - l. J. Klobuchar, P. Bernhardt, and J. Reisert, "Amateur Radio/HAM Studies of HEAO-Hole Effects"
 - m. C. Rush and D. Sarrazin, "ITS Studies of the HEAO-Hole"
 - n. J. Zinn, "Ground-Based Airglow Measurements of the HEAO-Hole"
 - o. D. Uffelman, "Preliminary Results from the NRL-MADRE HF Radar for the HEAO-C Launch"
 - p. P. Bernhardt, "Condensation of Rocket Exhausts"
 - q. D. Anderson, "Theoretical Modeling of Modification Effects"
 - r. M. Cousins, "TEC Modifications and Scintillations due to HEAO-C Launch Observed via LES-8 and LES-9 from Bermuda"
10. W. R. Wadt, "Simple Ideas Concerning Dissociative Recombination of H_2O^+ : Implications for $O(^1D)$ and $OH(^2\Sigma^+)$ Production," EOS 59, 334 (April 1978).
11. H. Volland and H. G. Mayr, "A Numerical Study of Three-Dimensional Diurnal Variations within the Thermosphere," Ann. Geophys. 29, 61-75 (1973).
12. J. M. Forbes and H. B. Garrett, "Solar Diurnal Tide in the Thermosphere," J. Atmos. Sci. 33, 2226 (1976).
13. J. M. Forbes and H. B. Garrett, "Seasonal-Latitudinal Structure of the Diurnal Thermospheric Tide," J. Atmos. Sci. 35, 148-159 (1978).
14. H. B. Garrett and J. M. Forbes, "Tidal Structure of the Thermosphere at Equinox," J. Atmos. and Terr. Phys. 40, 657-668 (1978).
15. R. G. Roble, R. E. Dickinson, and E. C. Ridley, "Seasonal and Solar Cycle Variations of the Zonal Mean Circulation in the Thermosphere," J. Geophys. Res. 82, 5493-5504 (1977).
16. R. M. Harper, "A Semidiurnal Tide in the Meridional Wind at F-Region Heights at Low Latitudes," J. Geophys. Res. 84, 411-415 (1979).
17. Paul A. Bernhardt, "The Response of the Ionosphere to the Injection of Chemically Reactive Vapors," Stanford Electronics Laboratories Technical Report No. 17 (SEL-76-009) (May 1976).
18. R. C. Molander and H. G. Wolfhard, "Explanation of Large Apollo-8 (J-2) Rocket Plume Observed during Trans-Lunar Injection," Institute for Defense Analysis Note N-610, IDA Log #HQ 69-9734 (February 1969).
19. M. B. Pongratz, G. M. Smith, C. D. Sutherland, and J. Zinn, "LAGOPEDO - Two F-Region Ionospheric Depletion Experiments," presented at American Geophysical Union 1978 Spring Meeting, Miami, FL (March 1978).
20. Paul A. Bernhardt, "High-Altitude Vapor Releases: Expansion with Condensation," contained in "Ionospheric Modification by Rocket Effluents, Final Report," Radioscience Laboratory, Stanford University Technical Report E326-2 (June 1, 1980).

21. S. P. Zimmerman and E. A. Murphy, "Stratospheric and Mesospheric Turbulence," in Proc. NATO Advanced Study Institute - Dynamical and Chemical Coupling, B. Grandal and J. A. Holtet, eds. (D. Reidel Publishing Co., Dordrecht, Holland, 1977), p. 35-47.
22. M. Ackerman, "Ultraviolet Radiation Related to Mesospheric Processes," in Mesospheric Models and Related Experiments, Fiocco (ed), (D. Reidel Publishing Co., Dordrecht, Holland, 1971).
23. L. Heroux and H. E. Hinteregger, "Aeronomical Reference Spectrum for Solar UV below 2000 Å," J. Geophys. Res. 83, 5305-5308 (1978).
24. Marsha R. Torr, D. G. Torr, R. A. Ong, and H. E. Hinteregger, "Ionization Frequencies for Major Thermospheric Constituents as a Function of Solar Cycle 21," Geophys. Res. Lett. 6, 771-774 (October 1979).
25. P. M. Banks and G. Kockarts, Aeronomy (Academic Press, NY, 1973).
26. L. G. Jacchia, "Atmospheric Models in the Region from 110 to 2000 km," Cospar International Reference Atmosphere report CIRA-1972, part 3, 227-338 (Akademie-Verlag, Berlin, 1972).
27. R. M. Harper, unpublished work.
28. P. Amayenc, "Tidal Oscillations of the Meridional Neutral Wind at Midlatitudes," Radio Sci. 9, 281-293 (1974).

NOTES ADDED IN PROOF

This report has been peer-reviewed in accordance with DoE SPS Project Office requirements. Reviewers included

Dr. Donald M. Rote, Argonne National Lab.,
 Dr. R. C. Whitten, NASA Ames Research Lab.,
 Dr. Paul A. Bernhardt, Stanford Electronics Lab.,
 Dr. R. P. Turco, R&D Associates,
 Dr. Michael Mendillo, Boston University, and
 Dr. Jeffrey Forbes, Boston College.

We have touched lightly on the subjects of noctilucent clouds, high-altitude contrails, and D-layer chemistry. These matters are treated in more detail in a report by R. C. Whitten, R. P. Turco, W. J. Borucki, S. S. Prasad, C. Park, L. A. Capone, C. A. Riegel, L. Pfister, H. T. Woodward, and T. Kropp, "Environmental Impact of the Satellite Power System on the Middle Atmosphere - an Assessment," to be published by US DoE SPS Project Office.